
# DUAL SOURCE WAVEGUIDE DESIGN FOR MATERIAL MEASUREMENT

THESIS

Daniel K. Koch, Capt, USAF

AFIT-ENG-MS-18-M-039

**DEPARTMENT OF THE AIR FORCE**
**AIR UNIVERSITY**

***AIR FORCE INSTITUTE OF TECHNOLOGY***

**Wright-Patterson Air Force Base, Ohio**

AFIT-ENG-MS-18-M-039

# DUAL SOURCE EXCITATION RECTANGULAR WAVEGUIDE DESIGN AND EVALUATION FOR THE MEASUREMENT OF ELECTROMAGNETIC MATERIAL PROPERTIES

THESIS

Presented to the Faculty

Department of Electrical and Computer Engineering

Graduate School of Engineering and Management

Air Force Institute of Technology

Air University

Air Education and Training Command

in Partial Fulfillment of the Requirements for the

Degree of Master of Science in Electrical Engineering

Daniel K. Koch, B.S.E.E.

Capt, USAF

March 2018

AFIT-ENG-MS-18-M-039

# DUAL SOURCE EXCITATION RECTANGULAR WAVEGUIDE DESIGN AND EVALUATION FOR THE MEASUREMENT OF ELECTROMAGNETIC MATERIAL PROPERTIES

THESIS

Daniel K. Koch, B.S.E.E.
Capt, USAF

Committee Membership:

Dr. Michael Havrilla
Chair

Dr. Peter Collins
Member

Dr. Julie Jackson
Member

AFIT-ENG-MS-18-M-039

# Abstract

Broadband material parameter measurements are essential in understanding how materials interact with electromagnetic waves. Traditional rectangular waveguide material measurement systems are bandwidth limited. This results in multiple rectangular waveguides of different sizes used to conduct broadband material parameter extraction. Efforts to produce a broadband rectangular waveguide have focused on the inclusion of different guiding structures in the waveguide body. These designs have the drawback of requiring precise machining and time-consuming sample preparation. This research proposes a new broadband rectangular waveguide design which uses a dual source excitation design. This is enabled by the fact that rectangular waveguides are linear time invariant systems. The fields excited by each source superimpose in a linear fashion. As a result, specific electromagnetic modes are suppressed. The single electromagnetic mode frequency range now depends on the relative phase of the excitation sources rather than the cutoff frequency of higher order modes.

A dual source excitation S-band waveguide is proposed in this research. Results from CST Microwave Studio® (MWS®) simulations are compared with those from a physical design measured with a 2-port network analyzer. These results are used to determine if this proposed rectangular waveguide design is suitable for broadband material measurements.

*To my wife and my family both near and far away.*

# Acknowledgements

I need to thank many people for their significant contributions to this research effort. From AFIT I'd like to thank Dr. Havrilla for his patience and guidance - his expertise is second to none, Maj Adam Brooks and Capt Joseph Ellis for their key assistance and feedback on my modeling and analysis process, and the AFIT Modeling and Fabrication Shop for their rapid response to my work requests. From AFRL I'd like to thank Mr. Alex Knisley for his vital modeling and simulation insight and suggestions, Mr. Jeff Massman for his material insight and 3D printed waveguide materials and the AFRL Maker Hub for giving me access to state of the art additive manufacturing machines, and Mr. Justin Wheatcroft and his team for their fantastic work measuring and evaluating the physical waveguide models produced. Without these people none of this research would be possible.

Daniel K. Koch

# Table of Contents

Page

# List of Figures

Figure Page

Figure Page

# List of Tables

DUAL SOURCE EXCITATION RECTANGULAR WAVEGUIDE DESIGN AND EVALUATION FOR THE MEASUREMENT OF ELECTROMAGNETIC MATERIAL PROPERTIES

# I. Introduction

Dielectric and magnetic materials are essential components in microwave systems. These materials have constitutive parameters known as relative permittivity ($\epsilon_r$) and permeability ($\mu_r$). These complex-valued parameters describe the ability of a material to support an electric polarization or a magnetization current density, respectively. The real part of the permittivity and permeability values characterizes field energy stored by the material and the imaginary part characterizes thermal energy losses.

Nicolson and Ross proposed a method for extracting the relative permittivity and permeability of a material in 1970 with the use of a network analyzer and sub-nanosecond pulses [29]. Their method uses a transmission line with a sample inserted in the center. The Fourier transform of the transmitted and reflected time-domain pulses is used to calculate the permittivity and permeability of the sample. Weir later improved this method and proposed what is known today as the Nicolson-Ross-Weir (NRW) method [43]. The NRW method uses frequency domain scattering parameters to determine the transmission and reflection coefficients of a sample to calculate the material's constitutive parameters.

The NRW method does not rely on a specific transmission line type. As a result, both circular waveguides and rectangular waveguides are used to extract material parameters. Circular waveguides provide a large frequency range over which measurements can be taken. The circular design makes material sample preparation

challenging. Rectangular waveguides on the other hand have a simple geometry, can handle high power levels, and have simple closed form solutions for traveling wave fields [26].

## 1.1 Problem Statement

The primary drawback to using rectangular waveguides to extract material parameters is the limited frequency range over which they can operate [26]. This is because transmission systems like waveguides and are designed to operate with a single electromagnetic mode excited. The single-mode operational frequency regime of a rectangular waveguide is determined by the interior dimensions of the waveguide. After the dominant mode is excited, unwanted higher order modes are excited as the input frequency increases. Once the excitation frequency exceeds the maximum of the single mode range, higher order electromagnetic modes can exist and subsequently interfere with dominant mode propagation. This degrades the waveguide's power transfer capability and thus the ability to measure the scattering parameters of the sample. If measurements outside the single mode frequency range are desired, multiple material samples must be prepared for waveguides of different interior dimensions.

Rectangular waveguides are linear systems. If two excitation sources are placed in the waveguide, the fields excited by each source will superimpose in a linear manner [32]. Two sources can be excited simultaneously or sequentially and produce the same results after the appropriate conversions are conducted. Using a dual source excitation scheme (i.e., common or differential mode excitation), the fields of specific electromagnetic modes will superimpose constructively while others will superimpose destructively. This leads to the suppression of certain electromagnetic modes [13]. Ultimately, the single mode operational frequency range can be improved for a rect-

angular waveguide with this dual source excitation design.

## 1.2 Previous Work

The application of rectangular waveguides in material parameter extraction goes further than single dielectric samples [2] [15]. Rectangular waveguides are used to extract complex electromagnetic material properties of layered dielectric samples [8],and biaxial materials [9] [22] as well. Each of these works uses the scattering parameters measured by a network analyzer to approximate $\epsilon_r$ and $\mu_r$.

Broadband rectangular waveguides have been proposed by many different authors. Saha and Guha propose L-shaped and T-shaped septa of varying dimensions depicted in Figure 1. Experimental data confirms that a proposed L-shaped septa design improves the bandwidth of the rectangular waveguide over 133% [37]. Other stub, L-shaped, and T-shaped septa designs are considered by Rong and Zaki. They show the relationship between septa placement, size, and symmetry for nine different designs. Each design has tradeoffs in terms of power-handing, bandwidth, attenuation, dominant mode cutoff wavelength, and characteristic impedance [34]. Hyde and Havrilla propose a broadband nondestructive method for characterizing magnetic materials using a clamped dual ridge waveguide. The dual ridge waveguide has a significant single mode operational frequency range of 6 to 18 GHz [18]. This material measurement technique requires the use of a large flat sheet of the material under test, which is a departure from the relatively small samples transitionally used in material parameter measurements.

All of the above designs show to varying degrees how structures included in the guiding section of a rectangular waveguide can improve the overall single mode frequency range. The issue with these designs is the challenge to accurately manufacture septa designs and prepare material samples for these designs. Further, it cannot be

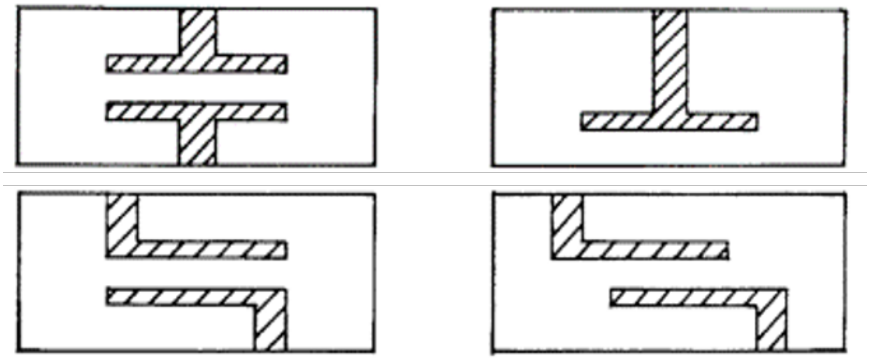

**Figure 1. Different septa designed to increase rectangular waveguide single mode operation frequency range [37].**

ignored that expressions for the electromagnetic fields excited in these structures are far more complicated than those excited in a traditional rectangular waveguide.

### 1.3 Goals

The goal of this research is to simulate, design, and test a dual source excitation rectangular waveguide and determine whether it can be used in broadband material characterization. This is accomplished with iterative CAD designs in CST MWS®. Design parameters are determined from these simulations and a physical model is manufactured and tested in order to validate simulation data. Simulation and physical testing has two focuses: the efficiency with which the waveguide launcher can transmit power and the accuracy with which the system can extract material properties.

### 1.4 Scope

The scope of this research is the application of the designed rectangular waveguide in the electromagnetic measurement of materials. The rectangular waveguide will not contain tuning structures for improved coax-to-waveguide transition. While these structures can improve the overall performance of the waveguide, the manufacture

and numerical analysis of these structures is outside the scope of this research effort. Only simple dielectric media which can be 3D printed is used for parameter extraction. These are limited to epoxy resin due to the available 3D printers.

## 1.5 Challenges

Due to the time constraint associated with this research, only a single physical model will be produced. This means any errors or design flaws will not be addressed via the production of a second model. Efforts will be taken to ensure that the physical model produced matches as closely to the CAD simulated model. Wire electrical discharge machining (EDM) will be used to produce orthogonal, axially-aligned interior surfaces on the physical model.

In order to transition the CAD model analyzed in CST MWS® to one which can be manufactured, certain design changes will be made. Efforts will be taken to ensure that, despite these changes, the function of the waveguide system is not impacted.

The samples used in this research will be 3D printed. A certain amount of deformation occurs during and after the epoxy resin has cured. These deformations will manifest in the measurements as a source of error. Efforts will be made to ensure that the samples are as flat as possible to reduce this source of error.

## 1.6 Resources

The Air Force Institute of Technology (AFIT) Low Observable Radar Electromagnetic Network (LOREnet) possesses CST Microwave Studio® (MWS®) licenses required to design and evaluate potential rectangular waveguide models. Analysis code will be generated to analyze simulated and test data using Matlab 2016b for which AFIT possesses academic licenses. The AFIT material measurement laboratory owns a two-port waveguide which is used in waveguide measurements. AFIT will

contract Triangle Precision Industries (TPI) located in Kettering, OH to manufacture an aluminum waveguide model. The AFRL Maker Hub possesses a FormLabs Form 2 stereolithography (SLA) 3D printer which can produce samples from epoxy resin.

## 1.7 Organization

In chapter II background information is provided to understand the basics of rectangular waveguide theory, network analyzer operation, and material measurement. Chapter III details the CAD model development process, calibration algorithm used, and material parameter extraction process used in this research. Chapter IV details the results of the CAD simulations and physical model measurements. Finally, Chapter V provides the pertinent takeaways from this effort along with future research recommendations.

# II. Background

A review of basic electromagnetic theory is required to understand the design and operations of rectangular waveguide systems. Much of this derivation relies on [4] and [31].

## 2.1 Maxwells Equations

The rigorous development of field equations for the electromagnetic modes which are excited and propagate in a rectangular waveguide starts with Maxwells equations describing the field behavior of an electromagnetic wave:

$$\nabla \times \vec{E} = -\vec{M} - j\omega\vec{B} \tag{1a}$$

$$\nabla \times \vec{H} = \vec{J} + j\omega\vec{D} \tag{1b}$$

$$\nabla \cdot \vec{D} = \rho_e \tag{1c}$$

$$\nabla \cdot \vec{B} = \rho_m \tag{1d}$$

where $\vec{E}$ is the electric field, $\vec{M}$ is the magnetic current density, $\vec{B}$ is the magnetic flux density, $\vec{H}$ is the magnetic field, $\vec{J}$ is the electric current density, $\vec{D}$ is the electric flux density, $\rho_e$ is the electric charge density, and $\rho_m$ is the magnetic current density. The auxiliary relationships for simple media are

$$\vec{B} = \mu\vec{H} \tag{2a}$$

$$\vec{D} = \epsilon\vec{E} \tag{2b}$$

where $\mu = \mu_r\mu_0$ and $\epsilon = \epsilon_r\epsilon_0$. The terms $\epsilon_r$ and $\epsilon_0$ are the relative and vacuum permittivity respectively while $\mu_r$ and $\mu_0$ are the relative and vacuum permeability. In the analysis of electromagnetic problems involving simple media, vector potentials

are often employed to simplify analysis and to identify Transverse Electric (TE) and Transverse Magnetic (TM) solutions. Vector potentials are discussed below.

**Magnetic Vector Potential.**

The magnetic vector potential $\vec{A}$ for simple media may be identified by first removing the magnetic sources from Maxwell's equations, namely

$$\nabla \times \vec{E}_A = -j\omega\mu\vec{H}_A \tag{3a}$$

$$\nabla \times \vec{H}_A = \vec{J} + j\omega\epsilon\vec{E}_A \tag{3b}$$

$$\nabla \cdot \vec{D}_A = \rho_e \tag{3c}$$

$$\nabla \cdot \vec{B}_A = 0 \tag{3d}$$

The Gauss's law $\nabla \cdot \vec{B}_A = 0$ implies that $\vec{B}_A$ must be purely solenoidal, thus,

$$\vec{B}_A = \mu\vec{H}_A = \nabla \times \vec{A} \tag{4}$$

or

$$\vec{H}_A = \frac{1}{\mu}\nabla \times \vec{A} \tag{5}$$

Substituting Equation (5) into Faraday's law expressed in terms of $\vec{A}$ (Equation (3a)) produces

$$\nabla \times (\vec{E}_A + j\omega\vec{A}) = 0. \tag{6}$$

The vector identity $\nabla \times (-\nabla\phi_e) = 0$ implies that $\vec{E}_A + j\omega\vec{A} = -\nabla\phi_e$, where $\phi_e$ is the electric scalar potential and the minus sign is introduced by convention. Thus

$$\vec{E}_A = -\nabla\phi_e - j\omega\vec{A}. \tag{7}$$

Substituting Equations (5) and (7) into Ampere's law (Equation (3b)), applying the vector identity $\nabla \times \nabla \times \vec{A} = \nabla(\nabla \cdot \vec{A}) - \nabla^2 \vec{A}$, and using the Lorenz Gauge $\nabla \cdot \vec{A} = -j\omega\epsilon\mu\phi_e$ leads to the following wave equation for $\vec{A}$:

$$\nabla^2 \vec{A} + k^2 \vec{A} = -\mu \vec{J} \tag{8}$$

where $k^2 = \omega^2 \epsilon\mu$. Implementing the Lorenz Gauge into Equation (7) allows the electric field to be written as

$$\vec{E}_A = -j\omega\vec{A} - j\frac{1}{\omega\mu\epsilon}\nabla(\nabla \cdot \vec{A}). \tag{9}$$

**Electric Vector Potential.**

The electric vector potential $\vec{F}$ for simple media may be identified by first removing the electric sources from Maxwell's equations, namely

$$\nabla \times \vec{E}_F = -\vec{M} - j\omega\mu\vec{H}_F \tag{10a}$$

$$\nabla \times \vec{H}_F = j\omega\epsilon\vec{E}_F \tag{10b}$$

$$\nabla \cdot \vec{D}_F = 0 \tag{10c}$$

$$\nabla \cdot \vec{B}_F = \rho_m \tag{10d}$$

The Gauss's law $\nabla \cdot \vec{D}_F = 0$ implies that $\vec{D}_F$ must be purely solenoidal, thus,

$$\vec{D}_F = \epsilon\vec{E}_F = \nabla \times \vec{F} \tag{11}$$

or

$$\vec{E}_F = \frac{1}{\epsilon}\nabla \times \vec{F}. \tag{12}$$

Substituting Equation (12) into Faraday's law expressed in terms of $\vec{F}$ (Equation

(10b)) produces

$$\nabla \times (\vec{H}_F + j\omega\vec{F}) = 0 \tag{13}$$

The vector identity $\nabla \times (-\nabla\phi_m) = 0$ implies that $\vec{H}_F + j\omega\vec{F} = -\nabla\phi_m$ where $\phi_m$ is the magnetic scalar potential and the minus sign is introduced by convention. Thus,

$$\vec{H}_F = -\nabla\phi_m - j\omega\vec{F}. \tag{14}$$

Substituting Equations (12) and (14) into Ampere's law expressed in terms of $\vec{A}$ (Equation (10a)), applying the vector identity $\nabla \times \nabla \times \vec{F} = \nabla(\nabla \cdot \vec{F}) - \nabla^2\vec{F}$, and using the Lorenz Gauge $\nabla \cdot \vec{F} = -j\omega\epsilon\mu\phi_m$ leads to the following wave equation for $\vec{F}$:

$$\nabla^2\vec{F} + k^2\vec{F} = -\epsilon\vec{M} \tag{15}$$

where $k^2 = \omega^2\epsilon\mu$. Implementing the Lorenz Gauge into Equation (14) allows the magnetic field to be written as

$$\vec{H_F} = -j\omega\vec{F} - j\frac{1}{\omega\mu\epsilon}\nabla(\nabla \cdot \vec{F}). \tag{16}$$

**Field recovery summary.**

As a result of introducing the vector potentials, we can express the total electric and magnetic fields in terms of $\vec{A}$ and $\vec{F}$:

$$\vec{E} = \vec{E_A} + \vec{E_F} = -j\omega\vec{A} - j\frac{1}{\omega\mu\epsilon}\nabla(\nabla\cdot\vec{A}) - \frac{1}{\epsilon}\nabla\times\vec{F} \tag{17a}$$

$$\vec{H} = \vec{H_A} + \vec{H_F} = \frac{1}{\mu}\nabla\times\vec{A} - j\omega\vec{F} - j\frac{1}{\omega\mu\epsilon}\nabla(\nabla\cdot\vec{F}) \tag{17b}$$

or, more generally,

$$\begin{aligned}\vec{E} = \hat{x}[&-j\omega A_x - j\frac{1}{\omega\mu\epsilon}(\frac{\partial^2 A_x}{\partial x^2} + \frac{\partial^2 A_y}{\partial x\partial y} + \frac{\partial^2 A_z}{\partial x\partial z}) - \frac{1}{\epsilon}(\frac{\partial F_z}{\partial y} - \frac{\partial F_z}{\partial z})]\\ + \hat{y}[&-j\omega A_y - j\frac{1}{\omega\mu\epsilon}(\frac{\partial^2 A_x}{\partial x\partial y} + \frac{\partial^2 A_y}{\partial y^2} + \frac{\partial^2 A_z}{\partial y\partial z}) - \frac{1}{\epsilon}(\frac{\partial F_x}{\partial z} - \frac{\partial F_z}{\partial x})]\\ + \hat{z}[&-j\omega A_z - j\frac{1}{\omega\mu\epsilon}(\frac{\partial^2 A_x}{\partial x\partial z} + \frac{\partial^2 A_y}{\partial y\partial z} + \frac{\partial^2 A_z}{\partial z^2}) - \frac{1}{\epsilon}(\frac{\partial F_y}{\partial x} - \frac{\partial F_x}{\partial y})]\end{aligned} \tag{18}$$

and

$$\begin{aligned}\vec{H} = \hat{x}[&-j\omega F_x - j\frac{1}{\omega\mu\epsilon}(\frac{\partial^2 F_x}{\partial x^2} + \frac{\partial^2 F_y}{\partial x\partial y} + \frac{\partial^2 F_z}{\partial x\partial z}) + \frac{1}{\mu}(\frac{\partial A_z}{\partial y} - \frac{\partial A_z}{\partial z})]\\ + \hat{y}[&-j\omega F_y - j\frac{1}{\omega\mu\epsilon}(\frac{\partial^2 F_x}{\partial x\partial y} + \frac{\partial^2 F_y}{\partial y^2} + \frac{\partial^2 F_z}{\partial y\partial z}) + \frac{1}{\mu}(\frac{\partial A_x}{\partial z} - \frac{\partial A_z}{\partial x})]\\ + \hat{z}[&-j\omega F_z - j\frac{1}{\omega\mu\epsilon}(\frac{\partial^2 F_x}{\partial x\partial z} + \frac{\partial^2 F_y}{\partial y\partial z} + \frac{\partial^2 F_z}{\partial z^2}) + \frac{1}{\mu}(\frac{\partial A_y}{\partial x} - \frac{\partial A_x}{\partial y})]\end{aligned} \tag{19}$$

in rectangular coordinates. This is advantageous when analyzing the fields excited in a rectangular waveguide due to the geometry of the guiding structure.

## 2.2 Transverse Electromagnetic Wave Solutions

In order the derive the transverse electromagnetic wave relationships a coordinate system must first be established. Figure 2 depicts the orthogonal coordinate system which is used going forward.

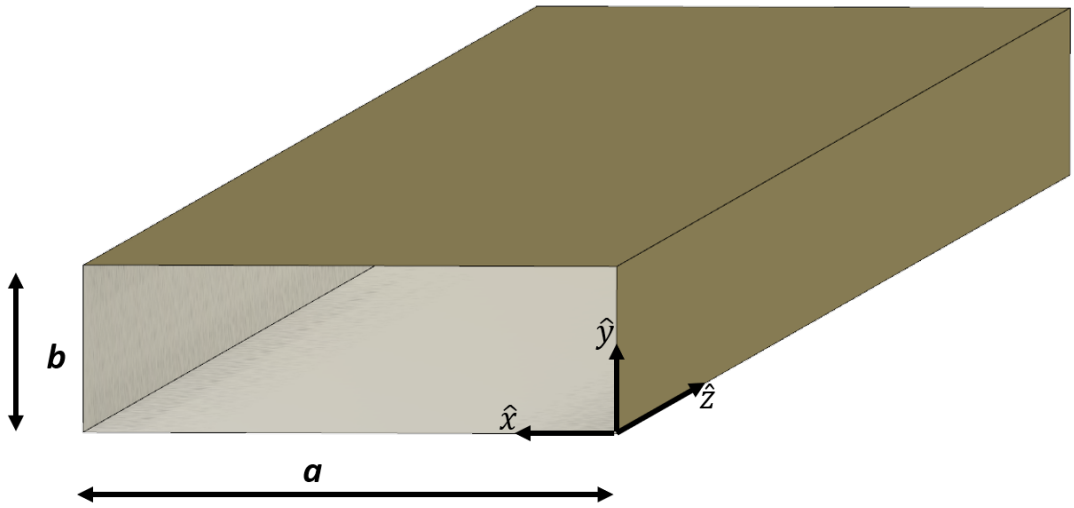


**Figure 2. Rectangular waveguide body section with coordinate system.**

There are three primary types of modes which result from Equation 17: TE, TM, and Transverse Electromagnetic (TEM). While the following section derives the field components for TE and TM modes in a rectangular waveguide, TEM modes are not supported in a waveguide with this geometry. This is due to the enforcement of the boundary conditions along the walls of the waveguide in conjunction with the fields which set up in the $\hat{x}$, $\hat{y}$, and $\hat{z}$ directions [25]. There are important relationships which must be defined regarding modes propagating in a waveguide: the field component equations of the modes, the cutoff frequency ($f_c$) of a mode, and the wave impedance ($\mathrm{Z}_w$) of a mode.

**Transverse Electric Modes.**

Transverse electric modes are those for which the electric field lies only in the plane transverse to the direction of propagation. For modes traveling in the $\hat{z}$ direction this results in $E_x$, $E_y \neq 0$ while $E_z = 0$. Further, TE modes are generated in the absence of a magnetic field source. As a result, the magnetic vector potential $\vec{A} = 0$ and the magnetic flux density $\vec{M} = 0$. It is seen from Equation 17a that $\vec{F} = \hat{z}F_z$ is the

generator for TE$^z$ modes. The corresponding wave equation becomes

$$\nabla^2 F_z(x,y,z) + k^2 F_z(x,y,z) = 0 \tag{20}$$

where, by using the separation of variables method for solving differential equations, $F_z$ becomes the product of three orthogonal equations, namely: $f(x)$, $g(y)$, and $h(z)$. Taking into consideration the waveguide geometry in Figure 2, we know that a standing wave will set up in the $\hat{x}$ and $\hat{y}$ directions while a traveling wave must set up in the $\hat{z}$ direction. Standing waves are expressed as the superposition of sinusoidal functions, whereas traveling waves are expressed as the superposition of exponential functions. This results in a general expression for a mode traveling in the $+\hat{z}$ direction of

$$F_z^+ = [C_1 \cos(k_x x) + D_1 \sin(k_x x)][C_2 \cos(k_y y) + D_2 \sin) k_y y)] A_3 e^{-jk_z z} \tag{21}$$

where $k_x^2 + k_y^2 + k_z^2 = k^2$ and the values $A_3$, $C_1$, $C_2$, $D_1$, and $D_2$ are arbitrary scalar coefficients. Equation (17) now becomes $\vec{E} = -\frac{1}{\epsilon}\nabla \times \vec{F}$ and $\vec{H} = -j\omega\vec{F} - j\frac{1}{\omega\mu\epsilon}\nabla(\nabla \cdot \vec{F})$ which results in

$$E_x = -\frac{1}{\epsilon}\frac{\partial F_z}{\partial y} \tag{22a}$$

$$E_y = \frac{1}{\epsilon}\frac{\partial F_z}{\partial x} \tag{22b}$$

$$E_z = 0 \tag{22c}$$

$$H_x = -j\frac{1}{\omega\mu\epsilon}\frac{\partial^2 F_z}{\partial x \partial z} \tag{22d}$$

$$H_y = -j\frac{1}{\omega\mu\epsilon}\frac{\partial^2 F_z}{\partial y \partial z} \tag{22e}$$

$$H_z = -j\frac{1}{\omega\mu\epsilon}(\frac{\partial^2}{\partial z^2} + k^2) F_z \tag{22f}$$

In order to get a unique solution, the boundary conditions of the walls of the

waveguide are enforced. Here, the Perfect Electric Conductor (PEC) walls force the tangential electric field component to zero when evaluated at the wall. This leads to the following conditions for the left and right walls

$$E_y(x = 0, 0 \leq y \leq b, z) = E_y(x = a, 0 \leq y \leq b, z) = 0 \tag{23a}$$

$$E_z(x = 0, 0 \leq y \leq b, z) = E_z(x = a, 0 \leq y \leq b, z) = 0 \tag{23b}$$

and for the top and bottom walls

$$E_x(0 \leq x \leq a, y = 0, z) = E_x(0 \leq x \leq a, y = b, z) = 0 \tag{24a}$$

$$E_z(0 \leq x \leq a, y = 0, z) = E_z(0 \leq x \leq a, y = b, z) = 0 \tag{24b}$$

As a result of enforcing these boundary conditions and selecting nontrivial solutions where appropriate, $D_1 = 0$, $D_2 = 0$, $k_x = \frac{m\pi}{a}$, and $k_y = \frac{n\pi}{b}$. Here, $m$ and $n$ are nonnegative integers where both $m$ and $n$ cannot be equal to zero simultaneously. These numbers specify the TE$^z$ mode for which Equations (23) and (24) are valid. The electric potential vector $F_z^+$ now simplifies to

$$F_z^+ = A_{mn}^+ cos(k_x x) cos(k_y y) e^{-jk_z z} \tag{25}$$

where $A_{mn}^+ = C_1 C_2 A_3$. Plugging Equation (25) into Equation (22) results in the mode

field component equations

$$E_x^+ = A_{mn}^+ \frac{k_y}{\epsilon} cos(k_x x) sin(k_y y) e^{-jk_z z} \tag{26a}$$

$$E_y^+ = -A_{mn}^+ \frac{k_x}{\epsilon} sin(k_x x) cos(k_y y) e^{-jk_z z} \tag{26b}$$

$$E_z^+ = 0 \tag{26c}$$

$$H_x^+ = A_{mn}^+ \frac{k_x k_z}{\omega\mu\epsilon} sin(k_x x) cos(k_y y) e^{-jk_z z} \tag{26d}$$

$$H_y^+ = A_{mn}^+ \frac{k_y k_z}{\omega\mu\epsilon} cos(k_x x) sin(k_y y) e^{-jk_z z} \tag{26e}$$

$$H_z^+ = -jA_{mn}^+ \frac{k_c^2}{\omega\mu\epsilon} cos(k_x x) cos(k_y y) e^{-jk_z z} \tag{26f}$$

where $k_c = \sqrt[2]{k_x^2 + k_y^2}$ and is the cutoff wavenumber for the $mn^{th}$ mode. This represents the wavenumber below which the $\text{TE}_{mn}$ mode will not propagate in a given rectangular waveguide. Alternatively, the cutoff frequency $f_c$ is the frequency below which modes will not propagate in a waveguide

$$(f_c)_{mn} = \frac{1}{2\pi\sqrt{\mu\epsilon}} \sqrt{\left(\frac{m\pi}{a}\right)^2 + \left(\frac{n\pi}{b}\right)^2} \tag{27}$$

Finally, the wave impedance for a particular mode $Z_w^{+z}(TE_{mn}) \equiv \frac{E_x^+}{H_y^+}$. The wave impedance can be expressed in terms of a ratio of the stimulus frequency and the cutoff frequency for a specific mode

$$Z_w^{+z}(TE_{mn}^z) = \frac{\eta}{\sqrt{1 - (\frac{f_c}{f})^2}} \tag{28}$$

where $\eta = \sqrt{\frac{\mu}{\epsilon}}$ and $f > f_{c(mn)}$.

**Transverse Magnetic Modes.**

Transverse magnetic modes are those which the magnetic field lies only in the plane transverse to the direction of propagation. As a result, the magnetic potential vector $\vec{F} = 0$, the electric flux density $\vec{J} = 0$ and the magnetic field component in the $\hat{z}$ direction $H_z = 0$. It is seen from Equation (17b) that $\vec{A} = \hat{z}A_z$ generates the TM$^z$ modes, thus the corresponding wave equation becomes

$$\nabla^2 A_z(x, y, z) + k^2 A_z(x, y, z) = 0 \tag{29}$$

where, by using the separation of variables method for solving differential equations, $A_z$ becomes the product of three independent and orthogonal equation namely, $f(x)$, $g(y)$, and $h(z)$. Taking into consideration the waveguide geometry in Figure 2, we know that a standing wave will set up in the $\hat{x}$ and $\hat{y}$ directions while a traveling wave must set up in the $\hat{z}$ direction. Here, the standing waves will be expressed as the superposition of sinusoidal functions, whereas the traveling wave will be expressed as the superposition of exponential functions. This results in a general expression for a wave traveling in the $+\hat{z}$ direction of

$$A_z^+ = [C_1 cos(k_x x) + D_1 sin(k_x x)][C_2 cos(k_y y) + D_2 sin)k_y y)]A_3 e^{-jk_z z} \tag{30}$$

where $k_x^2 + k_y^2 + k_z^2 = k^2$ and the values $A_3$, $C_1$, $C_2$, $D_1$, and $D_2$ are arbitrary scalar coefficients different from those used in Equation (21). Equation (17) now becomes

$\vec{E} = -j\omega\vec{A} - j\frac{1}{\omega\mu\epsilon}\nabla(\nabla \cdot \vec{A})$ and $\vec{H} = \frac{1}{\mu}\nabla \times \vec{A}$ which results in

$$E_x = -j\frac{1}{\omega\mu\epsilon}\frac{\partial^2 A_z}{\partial x \partial z} \tag{31a}$$

$$E_y = -j\frac{1}{\omega\mu\epsilon}\frac{\partial^2 A_z}{\partial y \partial z} \tag{31b}$$

$$E_z = -j\frac{1}{\omega\mu\epsilon}(\frac{\partial^2}{\partial z^2} + k^2)A_z \tag{31c}$$

$$H_x = \frac{1}{\mu}\frac{\partial A_z}{\partial y} \tag{31d}$$

$$H_y = -\frac{1}{\mu}\frac{\partial A_z}{\partial x} \tag{31e}$$

$$H_z = 0 \tag{31f}$$

In order to get a unique solution, the boundary conditions of the walls of the waveguide are enforced. The PEC walls force the tangential electric field component to zero when the field is evaluated at the wall. This implies that for the left and right walls

$$E_y(x = 0, 0 \leq y \leq b, z) = E_y(x = a, 0 \leq y \leq b, z) = 0 \tag{32a}$$

$$E_z(x = 0, 0 \leq y \leq b, z) = E_z(x = a, 0 \leq y \leq b, z) = 0 \tag{32b}$$

and for the top and bottom walls

$$E_x(0 \leq x \leq a, y = 0, z) = E_x(0 \leq x \leq a, y = b, z) = 0 \tag{33a}$$

$$E_z(0 \leq x \leq a, y = 0, z) = E_z(0 \leq x \leq a, y = b, z) = 0. \tag{33b}$$

As a result of enforcing these boundary conditions and selecting the nontrivial solution where appropriate, $C_1 = 0$, $C_2 = 0$, $k_x = \frac{m\pi}{a}$, and $k_y = \frac{n\pi}{b}$. Here, $m$ and $n$ are nonzero integers. These numbers are the mode number for which the expressions

are valid. The magnetic potential vector $A_z^+$ now simplifies to

$$A_z^+ = B_{mn}^+ sin(k_x x) sin(k_y y) e^{-jk_z z} \tag{34}$$

where $B_{mn}^+ = D_1 D_2 A_3$. Plugging Equation (34) into Equation (31) results in the mode field component equations

$$E_x^+ = -B_{mn}^+ \frac{k_x k_z}{\omega \mu \epsilon} cos(k_x x) sin(k_y y) e^{-jk_z z} \tag{35a}$$

$$E_y^+ = -B_{mn}^+ \frac{k_y k_z}{\omega \mu \epsilon} sin(k_x x) cos(k_y y) e^{-jk_z z} \tag{35b}$$

$$E_z^+ = -jB_{mn}^+ \frac{k_c^2}{\omega \mu \epsilon} sin(k_x x) sin(k_y y) e^{-jk_z z} \tag{35c}$$

$$H_x^+ = B_{mn}^+ \frac{k_y}{\mu} sin(k_x x) cos(k_y y) e^{-jk_z z} \tag{35d}$$

$$H_y^+ = -B_{mn}^+ \frac{k_x}{\mu} cos(k_x x) sin(k_y y) e^{-jk_z z} \tag{35e}$$

$$H_z^+ = 0 \tag{35f}$$

where $k_c = \sqrt[2]{k_x^2 + k_y^2}$ is the cutoff wavenumber for the $mn^{th}$ mode. This represents the wavenumber below which the $\text{TM}_{mn}$ mode will not propagate in a given waveguide. Similarly, the cutoff frequency $f_c$ is the frequency below which modes will not propagate in a rectangular waveguide.

### 2.3 Rectangular Waveguides

Rectangular waveguides are a special type of microwave transmission line. Transmission lines are designed to transport power efficiently from a generator to a load by analyzing the impedance and attenuation of a system. This is the same goal in designing a waveguide launcher. Impedance mismatches at the interface between two transmission lines creates unwanted power reflections. For waveguides this results

increased power reflection back to the input source. To reduce these reflections, the two system impedances must be matched. This maximizes the power coupled into the waveguide and minimizes unwanted power reflections [31].

The important considerations in waveguide load matching are the excitation pin design and characteristic impedance of the dominant TE mode. Excitation pins are designed for specific field coupling. In this research electric field coupling pins are used which are oriented in the $+\hat{y}$ direction. Pin placement within the waveguide also play a vital role in power coupling. This is explored further in this section. Finally, the characteristic impedance of the dominant mode is an important consideration. The wave impedance for TE modes in Equation (28) shows that each mode has a different wave impedance $Z_w^{+z}$. While the input frequency is greater than the dominant mode cutoff frequency, the wave impedance is greater than the intrinsic impedance of the medium which fills the waveguide $\eta$ [3].

**Rectangular Waveguide Launcher Design.**

The field component equations presented up to this point have been derived for observations external to the electromagnetic source. In actuality, the source of radiation which excites these fields is contained in the waveguide launcher. The waveguide launcher is designed to deliver the maximum amount of power to the waveguide system over a specific operating frequency [4]. This is accomplished through physical design parameters and, in some cases, fine tuning post production [41]. Figure 3 provides the coordinate system and parameters which will be referenced in this section.

Traditional waveguides are designed for single mode operation which is determined by the cutoff frequencies for the first two electromagnetic modes excited in a waveguide with a specific interior width ($a$) and interior height ($b$) [31]. As long as $a > b$, the first mode excited will always be $\mathrm{TE}_{10}$. For waveguides where $a = 2b$, the first two

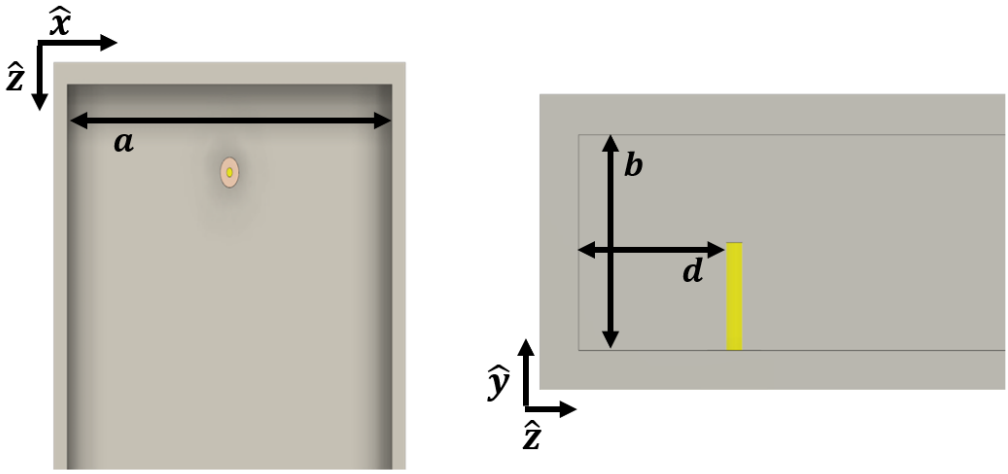


**Figure 3. Basic single source excitation rectangular waveguide launcher.**

electromagnetic modes which will be excited are $TE_{10}$ and $TE_{20}$. These modes are convenient because only three field components are nonzero which are excited: $E_y$, $H_x$, and $H_z$. With this in mind, traditional rectangular waveguides maintain a single mode operating frequency range between the cutoff frequencies of the $TE_{10}$ and $TE_{20}$ modes. The first step in designing a rectangular waveguide launcher for operation over a specific frequency range is to determine the interior dimension $a$ and $b$ such that only the $TE_{10}$ mode is excited over this frequency range.

Efficient power coupling into a waveguide designed for $TE_{10}$ single mode operation starts with the placement of the excitation pin. Excitation pins are traditionally thin $\hat{y}$-oriented wires. Because the maximum of the $E_y$ standing wave occurs where $x = a/2$, the excitation pin is placed in the center of the XY-plane in launcher. This is akin to plucking a string which is strung between two fixed points in the center. The next design consideration is the pin distance from the back PEC wall. This is traditionally set at $\lambda_z/4$ where $\lambda_z$ is the wavelength along the z-axis and is evaluated at the center frequency of the desired operational frequency range [4]. This is done

because the excitation pin launches a traveling wave in the $+\hat{z}$ direction and the $-\hat{z}$ direction. The wave initially launched in the $-\hat{z}$ direction will be reflected by the back PEC wall. On reflection, the wave undergoes a 180° phase shift and begins traveling in the $+\hat{z}$ direction. Because the excitation pin is placed $\lambda_z/4$ away from the back wall, the initially $-\hat{z}$ directed wave will undergo a 360° phase shift once it travels back to the excitation pin where it constructively interferes with the already $+\hat{z}$ directed traveling wave [28].

Once the physical design parameters are set for a given waveguide launcher design, extra power coupling structures are often added into the waveguide. This is due to the impedance mismatch between the coax cable and the rectangular waveguide. The excitation pins inside a rectangular waveguide are modeled as dipole antennas [30], [44] and analyzed with image theory [33] or Method-of-Moments [19], [20]. In an effort to reduce the coax-to-waveguide mismatch, structures have been proposed such as dielectric sheaths around the excitation pin [21], tuning stubs [41], or shaping of the excitation pin itself [7, 11, 39]. Each transition structure placed in a waveguide comes with different benefits and drawbacks; no single design works in all applications. In addition to the possible excitation of higher order modes, these structures require an increased amount of rigorous field analysis in order to fully understand their impact [38]. While simulation data can predict the interaction of these structures with the excited field components, physical testing is required to validate the simulation data [16].

## 2.4 Field Component Superposition

The dual source excitation design relies on two excitation pins driven at the same time with identical signals either in phase or completely out of phase. Each of these sources excite electromagnetic fields which combine together through a process

called interference or superposition. Interference occurs constructively or destructively. Whether fields of the same frequency interfere constructively or destructively depends on the relative phase of each field. Fields which are completely out of phase interfere destructively and produce a field with a reduced amplitude. Field components of the same frequency and phase interfere constructively which results in a field with a greater amplitude. In a rectangular waveguide specific modes are excited as denoted with the $mn$ subscripts attached to the TE and TM modes. Figure 4 shows the $E_y$ field profile for the $TE_{10}$, $TE_{20}$ and $TE_{40}$ modes.

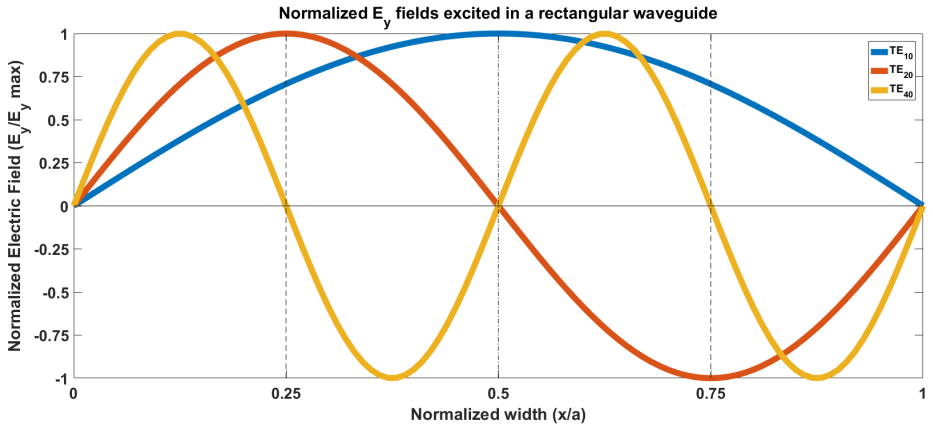


**Figure 4. Electric field profiles for select TE modes.**

The interaction of $E_y$ fields is of primary interest when considering a dual source excitation rectangular waveguide. Because we have mathematical expressions for the standing waves which are excited by the $E_y$ field components of the $TE_{m0}$ excited in a rectangular waveguide we can predict what the resultant $E_y$ field component will look like when two sources are placed in a waveguide launcher. Assuming that the excitation signal frequency is same for both excitation pins and the excitation pins are placed at an appropriate distance from the interior walls, the resultant $E_y$ field for $TE_{10}$ and $TE_{20}$ is depicted in Figure 5.

In this research, only two different excitation modes which are defined by their

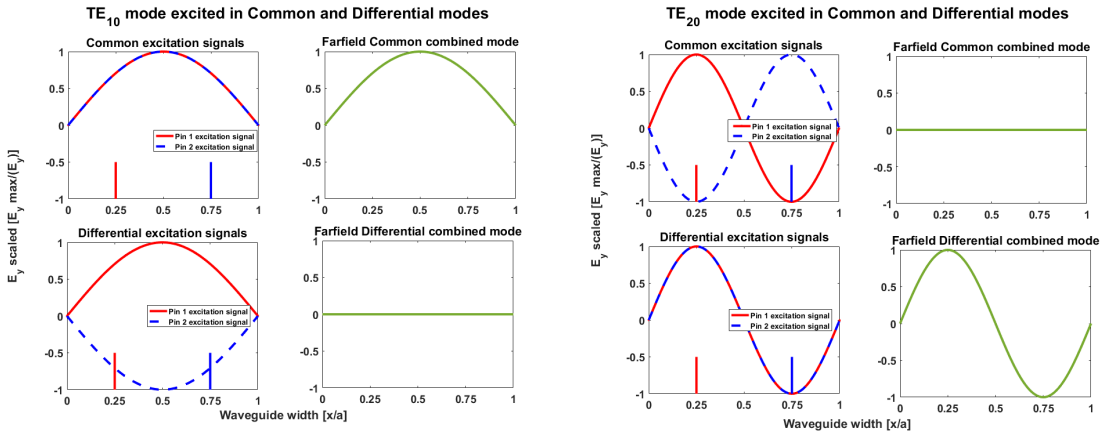


**Figure 5. Odd mode electric fields will be suppresses in differential excitation and even mode electric fields will be suppresses in common excitation mode.**

phase difference will be considered. These modes are Common (CC) where the phase difference is 0° and Differential (DD) where the phase difference is 180°. In CC mode, $TE_{m0}$ modes are suppressed where $m$ is even. The opposite is true of DD mode excitation, $TE_{m0}$ modes with an odd $m$ are suppressed. Physical placement of the excitation pins also inherently suppresses specific $TE_{m0}$ modes. In the case where the excitation pins are placed one quarter of the interior width of the waveguide away from the interior side walls the $TE_{40}$ mode is inherently prevented from coupling into the system. This is because the placement of an excitation pin at the null of the standing wave which is excited by a $E_y$ field component for an electromagnetic mode inhibits that mode from being excited in a waveguide [16]. Based on the mode suppression theory Table 1 summarizes the modes which will be suppressed by the symmetric placement of two excitation pins excited by two signals either completely in phase or completely out of phase.

## 2.5 Material Measurement

In order to extract the material parameters of a sample under test, the transmission and reflection coefficients of that material must be known. Network analyzers

**Table 1. Suppressed TE and TM modes in dual source waveguide. Common mode (CC) suppresses even $TE_{m0}$ modes while differential mode (DD) suppresses odd $TE_{m0}$ modes along with $TE_{40}$.**

| Mode | CC Excitation | DD Excitation |
|---|---|---|
| $TE_{10}$ | Unsuppressed | Suppressed |
| $TE_{20}$ | Suppressed | Unsuppressed |
| $TE_{30}$ | Unsuppressed | Suppressed |
| $TE_{40}$ | Suppressed | Suppressed |
| $TE_{50}$ | Unsuppressed | Suppressed |
| $TE_{01}$ | Suppressed | Suppressed |
| $TE_{11}$, $TM_{11}$ | Unsuppressed | Suppressed |
| $TE_{21}$, $TM_{21}$ | Suppressed | Unsuppressed |

can measure the scattering parameters of a rectangular waveguide with a sample inserted. The transmission and reflection coefficients of the sample are calculated by calibrating the S-parameters measured when the sample is placed in the waveguide. An understanding of how a network analyzer collects data and how material parameter extraction algorithms work will provide a motivation for steps detailed in Chapter III.

**Plane Wave Transmission and Reflection.**

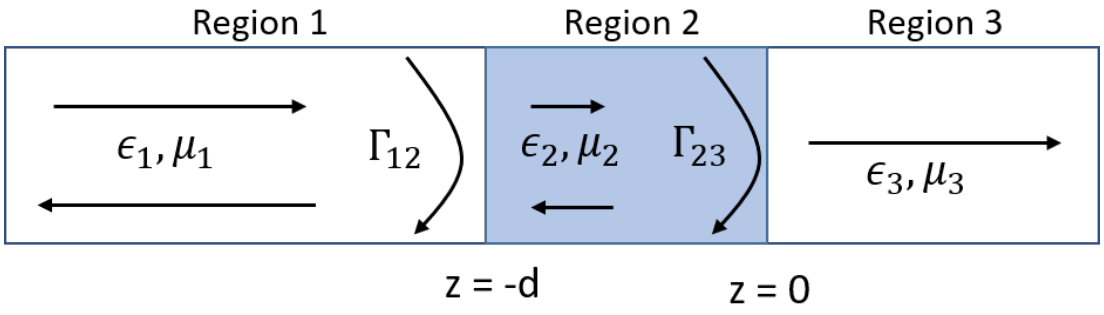


**Figure 6. Plane wave reflection coefficients and impedances used in rectangular waveguide material parameter extraction.**

In Figure 6, a plane wave travels in the $+\hat{z}$ direction from region 1 to region 3. As

the wave reaches the boundaries at $z = 0$ or $z = -d$ some of the wave is reflected ($\Gamma$) and some of the wave is transmitted ($T$). The reflection terms in the figure assume a steady state (i.e., they include the multiple reflections which occur as the plane wave reflects back and forth in the dielectric material). The reflection coefficient for a planar material interface is calculated with

$$\Gamma_{ij} = \frac{\eta_j - \eta_i}{\eta_j + \eta_i} \tag{36}$$

where $\Gamma$ is a complex value where $|\Gamma| < 1$ typically, $ij$ denotes the regions (i.e. 1, 2, 3, and so on), and $\eta = \sqrt[2]{\mu/\epsilon}$ and is the intrinsic impedance of a material. The relationship between reflection and transmission coefficients for lossless media is $T = 1 + \Gamma$. The total forward reflection coefficient ($\Gamma_{in}(z = -d^-)$ of the material under test determines the reflection S-parameter measured by a network analyzer. This is calculated with

$$\Gamma_{in} = \frac{\Gamma_{12} + \Gamma_{23} e^{-j2k_2 d}}{1 + \Gamma_{12}\Gamma_{23} e^{-j2k_2 d}} \tag{37}$$

where $k_2$ is the wavenumber in region 2. For dielectric materials $k_2 = \sqrt[2]{\omega\epsilon_0\epsilon_r\mu_0\mu_r - (k_c)^2}$, where $k_c$ is the dominant $\mathrm{TE}_{m0}$ mode cutoff wavenumber [3].

The forward reflection and transmission scattering parameters $\mathrm{S}_{11}$ and $\mathrm{S}_{21}$ respectively are related to the transmission and reflection coefficients with [1] and [10]

$$S_{11} = \Gamma_{in} \frac{1 - T_{in}^2}{1 - \Gamma^2 T^2} \tag{38a}$$

$$S_{21} = T_{in} \frac{1 - \Gamma_{in}^2}{1 - \Gamma^2 T^2} \tag{38b}$$

where $T_{in} = 1 - \Gamma_{in}$.

**Scattering Parameters.**

Network analyzers measure the scattering characteristics of microwave systems via S-parameters. S-parameters are calculated with

$$S_{ij} = \frac{b_i}{a_j} \tag{39}$$

where $i$ and $j$ are port numbers and $S_{ij}$ are the complex valued ratios of the power signal received on port $i$ ($b_i$) and the power signal sent from port $j$ ($a_j$) [31]. Two port network analyzers will generate four S-parameters: the reflection terms $S_{11}$ and $S_{22}$ and the transmission terms $S_{21}$ and $S_{12}$. Similarly, four port network analyzers generate 16 S-parameters; four reflection terms and 12 transmission terms. A useful feature of four port network analyzers is the ability to excite two ports at a time. This is done in common mode where the same signal is sent to both excitation ports at a time and differential mode where two signals completely out of phase are sent to the excitation ports [13].

**Electromagnetic Characterization of a Sample.**

When a electromagnetic wave (i.e., TEM, TE, or TM) traveling in a lossless media reaches a boundary, some of the energy in the wave is transmitted into the media while the rest is reflected and travels in the opposite direction. Two exceptions to this statement are perfect electric and magnetic conductors. Goring forward, it is assumed that the direction of travel is in the $+\hat{z}$ direction only and the angle of incidence is normal. The amount of energy reflected or transmitted depends on the difference in material properties between the two media (i.e. how much different the relative permittivities ($\epsilon_r$) and permeabilities ($\mu_r$) are) [3] .

The NRW method mentioned previously makes use of transmission and reflection

S-parameters in order to extract the relative permittivity and permeability of a sample under test. If all four S-parameters are available, the forward and reverse material parameters can be calculated. For simple media, these two values should be equal. This method is detailed in Appendix A.

An alternative method to NRW material parameter extraction makes use of the Newton's method for approximating the zeros of a function. Newton's method is an iterative method which required an initial guess ($x_0$) as to where the function $f(x) = 0$. The update equation used to better approximate the root of $f(x)$ is

$$x_{n+1} = x_n - \frac{f(x_n)}{f'(x_n)} \tag{40}$$

where $x_{n+1}$ is a better approximation for the root of $f(x)$. This method is used multiple times to improve on the approximation by using the calculated $x_{n+1}$ as the next guess in the function. A termination criteria is required in order for this method to finish if the previous $x_{n+1}$ is used as the current $x_n$. This can come in the form of a number of iterations completed or an accuracy determined by $|x_{n+1} - x_n|$. The number of iterations this method uses is dependent on the shape of the function $f(x)$, the accuracy of the initial guess, and desired accuracy. This method does not always converge to an answer as highly oscillatory functions or poorly selected initial guesses may prevent convergence [24].

The way in which the Newton Root Search method is used in electromagnetic material measurement is by using the theoretical and measured transmission ($T$) and reflection ($\Gamma$) coefficients

$$\Gamma(f, \epsilon, \mu)_{theoretical} - \Gamma(f)_{measured} = 0 \tag{41}$$

and

$$T(f, \epsilon, \mu)_{theoretical} - T(f)_{measured} = 0 \tag{42}$$

where $f$ is the frequency, and $\epsilon$, and $\mu$ are the values which are updated by Equation (40).

## 2.6 Computational Electromagnetics

This research makes use of the computational electromagnetic (CEM) software CST. CEM software solves complex electromagnetic problems by numerically solving Maxwell's equations. This is accomplished first by converting a CAD model of the problem into a set of nodes. This meshing process generates a set of points or nodes on which Maxwell's Equations are solved. Analysis is accomplished in either the transient domain with a finite difference time domain (FDTD) solver or in the frequency domain with a method of moment (MoM) or finite element method (FEM) solver. Each domain has key strengths and weaknesses in terms of computational resources, steady state solution, and meshing algorithms. The results from one solver should match those of an other. FDTD computations require a great amount of calculations while limiting the amount of computer memory used. On the other hand, MoM and FEM require a great amount of computer memory to numerically solve Maxwell's equations [42].

The CST MWS® transient domain solver is exclusively used in this research. This is done in order to compare the results from each solver for consistency. This is also done because the transient domain solver provides insight into time-based characteristics of the system under test. Transient domain simulations excite specific port(s) with a Gaussian pulse. This pulse contains a specific amount of power over the frequencies in the simulation domain. Results from this solver show a system's time-based response to an incident pulse and if an excitation pulse reflects back and

forth, or rings, in a system.

# III. Design and Evaluation Methodology

The first phase of this research is the design of a dual source excitation rectangular waveguide launcher. The model has three ports: two excitation pin ports and a port at the aperture of the waveguide. The aperture port is used to analyze the power delivered and modes excited by the pins. This phase relies on simulation data to refine the waveguide design parameters such as interior waveguide height and excitation pin distance from the back wall. The design parameters which deliver the most power over the largest bandwidth are used in subsequent research phases. The power coupling of the designed waveguide launcher is analyzed through a set of auxiliary simulations.

The second phase of research involves the simulation and physical testing of a two port model. The two port model is simply the three port model with a flat metal plate (reflection configuration) or a sample holder backed by a flat metal plate (sample configuration) placed at the aperture. This single sided waveguide model is used to extract the relative permittivity ($\epsilon_r$) of nonmagnetic dielectric material samples. In order to extract the $\epsilon_r$ of the material under test, the simulated and measured data must be calibrated. Calibration, whether applied to sample data or internally to the network analyzer, works to correct errors and set a reference plane [27]. After calibration, Newton's root search method is used to approximate $\epsilon_r$ by assuming that $\mu_r = 1$.

The third phase of research uses the two port model to create a four port or double-sided model. The double-sided model is a set of two port models connected together by their apertures. Double-sided configurations include *thru* in which nothing in placed between the apertures, *line* in which an empty sample holder is placed between the apertures, *reflection* in which a flat metal plate is placed between the apertures, and *sample* in which a sample holder filled with the sample under test is placed between the apertures. The first three configurations are used to calibrate

the data collected on the sample configuration. The calibrated data is then used to extract the forward and reverse relative permittivity and relative permeability. This is accomplished with both the Newton root search method and the NRW method.

Finally, a quantitative comparison of the transmission line metrics for all simulation and physical models is presented. This includes three port, two port, and four port models in each configuration simulated and tested. The quantitative basis of comparison are each model's mean return loss and mean insertion loss coefficients. The standing wave ratio is calculated for single sided and double sided models in the sample configurations.

## 3.1 Modeling and Simulation

Time and frequency domain data from simulations are analyzed for all models. In this research, the transient domain solver is preferred because of the time domain pulse information provided. Data collected from each simulation includes S-parameters (or F-parameters for the first phase three-port model which requires simultaneous excitation), time domain signals, and power accepted by each port. F-parameters are generated in CST when simultaneous excitation is used in the transient domain. These display the normalized power contained in each electromagnetic mode received by a port.

Uniform settings are used in each simulation to reduce the variability in CST results. In order to accurately mesh the CAD models, a maximum mesh node distance of $\lambda_{min}/10$ or 2.7 mm is set [42]. Simulation accuracy is set to -50 dB and adaptive mesh refinement is accomplished on each model to ensure stable solutions. The default Gaussian pulse is used as the excitation signal.

The three-port design begins with the model in Figure 7. The interior width ($a$) of the waveguide is set to 72.136mm and the interior height ($b$) is set at 16 mm to prevent

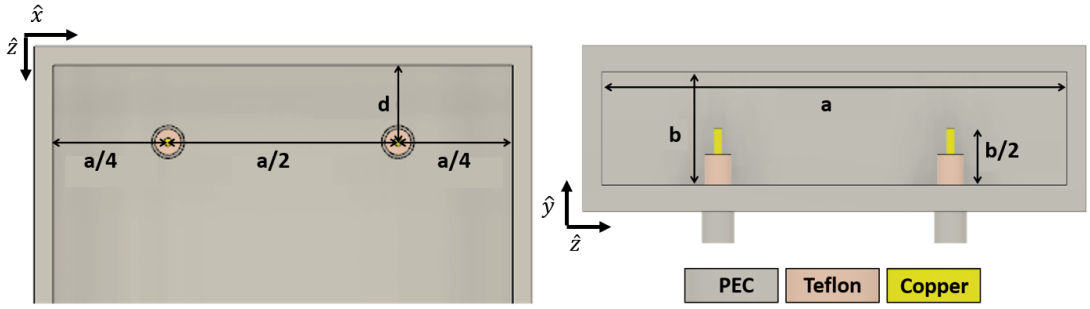


**Figure 7. Parameterized dual source excitation rectangular waveguide launcher modeled in CST MWS®.**

the excitation of higher order $TE_{mn}$ and $TM_{mn}$ modes. Parametric simulations are conducted in which the placement of the pins is varied in order to determine the most efficient distance ($d$) between excitation pins from the back wall of the waveguide. Three port model simulations are conducted with simultaneous excitation because of the aperture port. Subsequent models use individual excitation in order to mimic the way in which physical data is gathered. The design parameters determined from these parametric simulations are used to create a single-sided two port model and a double-sided four port waveguide model.

The way in which this system's power coupling capability is characterized is by a set of two simulations with the three port model. The first simulation uses only a single excitation pin. With this simulation the power reflected by the excitation pin is used to characterize the input power coupling of the system while the signal received by the non-excitation pin is used to characterize the crosstalk between excitation pins. The second simulation configuration uses the waveguide aperture as a single electromagnetic mode excitation source. Because common and differential excitation modes have different dominant electromagnetic mode frequency ranges, the aperture excites $TE_{10}$ over a specific frequency range and $TE_{20}$ over a different frequency range. The results from these two simulations characterize the efficiency with which single

$TE_{m0}$ mode power is coupled out of the waveguide.

For the latter two phases of this research, the two and four port models are simulated with individual excitations (i.e., each excitation pin is excited in turn rather than simultaneously). This allows for the conversion of single source S-parameters to two sets of dual source S-parameters. This has the added benefit of reducing by half the number of dual source simulations required.

Two port models include simulations with the reflection standard (i.e., flat metal plate) moved to different distances from the aperture of the waveguide. This is accomplished in order to calibrate data collected from sample configurations. Analysis on the S-parameters collected from the single sided configurations include both single and dual excitation. Single excitation analysis uses only the reflection S-parameters (i.e., $S_{mm}^{samp}$). Dual-source excitation uses all four S-parameters to generate $S_{11}^{CCorDD}$.

Four port models include the *thru*, *reflect*, and *line* configurations along with a dielectric *samp* configuration. The 16 S-parameters generated by each model configuration are converted to dual-source excitation S-parameters. The sample data is calibrated and material parameters are extracted.

### 3.2 Physical Measurements

Physical model measurements are collected with a two port Agilent network analyzer. Internal network analyzer calibration is accomplished to correct internal system noise, network analyzer port crosstalk, and to move the reference plane to the end of the network analyzer cables [12]. This results in measurements which mirror the simulation environment. In addition to calibrating the network analyzer, cable mismatch error terms must be corrected. This is done through the collection of 12 ratio measurements:

$$R_{uv} = \frac{a_u}{a_v}|_{\text{Port } v \text{ excitation}} \tag{43}$$

where $a_u$ and $a_v$ are the incident signals and $u$ and $v = 1, 2, 3, 4$ but $u \neq v$. These ratio measurements are used to find the actual S-parameters with the simple relationship:

$$S_{uv} = S^m_{uv} * R^{-1}_{uv} \tag{44}$$

where $S^m_{uv}$ are the measured S-parameters, $S_{uv}$ are the system detector S-parameters, and $R_{uv}$ are the ratios as defined by Equation (43).

The two port model is measured with the two network analyzer by collecting the four S-parameters and two ratio traces. The four port model requires six measurements in order to collect all 16 S-parameters and 12 ratios. This is accomplished by connecting the network analyzer cables to specific ports at a time with matched loads connected to the unused two ports. The six measurements collected are summarized in Table 2.

**Table 2. Two Port Network Analyzer Measurements. By taking six different measurements with a two port network analyzer, all 16 S-parameters for a four port dual source excitation waveguide are collected.**

| | Waveguide Ports | | | | | |
|---|---|---|---|---|---|---|
| **Measurement** | **1** | **2** | **3** | **4** | **S-parameters** | **Ratio** |
| 1 | I | II | L | L | $S_{11}$, $S_{12}$, $S_{21}$, $S_{22}$ | $R_{12}$, $R_{21}$ |
| 2 | I | L | II | L | $S_{13}$, $S_{31}$, $S_{33}$ | $R_{13}$, $R_{31}$ |
| 3 | I | L | L | II | $S_{14}$, $S_{41}$, $S_{44}$ | $R_{14}$, $R_{41}$ |
| 4 | L | I | II | L | $S_{23}$, $S_{32}$ | $R_{23}$, $R_{23}$ |
| 5 | L | I | L | II | $S_{24}$, $S_{42}$ | $R_{24}$, $R_{42}$ |
| 6 | L | L | I | II | $S_{34}$, $S_{43}$ | $R_{34}$, $R_{43}$ |
| I = network analyzer port 1<br>II = network analyzer port 2<br>L = matched load | | | | | | |

A 12 in/lb torque wrench is used to secure the cables to each of the 7 mm flange connectors. Two vice grips are used to apply pressure to the brackets holding the 7 mm flanges in place. A sweep time of no less than one second is used in each measurement. This is done to allow the excitation signal power to completely couple

out of the system before the next measurement is taken.

### 3.3 Material Measurement

Material measurement with a waveguide can be conducted in either single-sided or double-sided configurations. In single-sided measurements, the Newton root search method is used to extract $\epsilon_r$ from the calibrated sample data reflection coefficient $\Gamma$ in either single or dual excitation modes by assuming that $\mu_r = 1$ (i.e., the sample is nonmagnetic). In double-sided measurements both the NRW and Newton root search methods are used to extract the forward and reverse $\epsilon_r$ and $\mu_r$ of the sample under test from the calibrated data transmission ($T$) and reflection ($\Gamma$) coefficients. These processes are applied to both measurement and simulation data.

**Single-Sided Material Measurement.**

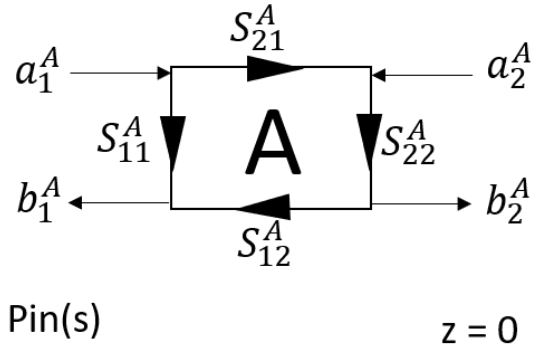


**Figure 8. A block diagram of the single sided waveguide model.**

Single-sided measurements are taken with the aperture of the waveguide connected to a flat plate or a sample holder backed by a flat plate at $z = 0$ in Figure 7. The sample holder can either be empty or filled with a sample under test. The block diagram of this model in Figure 8 depicts the waveguide as the system $A$. In the

single excitation scheme, the reflection S-parameters measured are modeled with

$$S_{11,p}^{ms} = S_{11}^{A} + \frac{S_{21}^{A} S_{12}^{A} S_{11,p}^{S}}{1 - S_{22}^{A} S_{11,p}^{S}} \tag{45}$$

where $S_{11,p}^{ms}$ is the measured reflection S-parameter with port $p$ excitation, $S_{11,p}^{S}$ is the reflection at $z = 0$, and $S_{mn}^{A}$ where $m, n = 1$ and 2 are the scattering parameters of the system $A$. $S_{11,p}^{ms}$ must be calibrated in order to determine the reflection coefficient at $z = 0$ (i.e., where the sample and waveguide aperture interface). There are three unknown terms in Equation (45): $S_{11}^{A}, S_{21}^{A} S_{12}^{A}$, and $S_{22}^{A}$. To solve for these terms, three standards with known $S_{11,p}^{S}$ values are required. These standards are generated by placing the flat plate at different distances away from the aperture. Empty sample holders of different thicknesses backed by a flat plate are measured or simulated. Because the reflection coefficient from a PEC plate is $-1$, the reflection coefficients from the different standards is determined by

$$S_{11,p}^{S} = -e^{j2k_{z0}L_s} \tag{46}$$

where $e^{j2k_{z0}L_s}$ represents a phase shift, $k_{z0} = \sqrt[2]{k_0 - k_c^2}$, $k_0 = \omega/c$, $\omega = 2\pi f$, $k_c = \frac{m\pi}{a}$, $m$ is the dominant mode number, $a$ is the waveguide width, and $L_s$ is the distance from the waveguide aperture to the flat plate. This calibration method outlined in Appendix B.

The Newton root search method used to extract $\epsilon_r$ from calibrated single sided data is

$$S_{11}^{T}(\epsilon_r, \omega) - S_{11}^{samp} = 0 \tag{47}$$

where $S_{11}^{samp}$ is the measured or simulated sample reflection S-parameter and $S_{11}^{T}$ is

the theoretical sample reflection calculated with

$$S_{11}^{T} = \frac{R(1-P^2)}{1-R^2P^2} \tag{48}$$

where $R = \frac{Z-Z_0}{Z+Z_0}$, $Z = \omega\mu_0/k_z$, $k_z = \sqrt[2]{\omega^2\epsilon\mu_0 - k_c^2}$, $k_c = \pi/a$, $a$ is the width of the rectangular waveguide in meters, $Z_0 = \omega\mu_0/k_{z0}$, $k_{z0} = \sqrt[2]{k_0^2 - k_c^2}$, $k_0 = \omega/c$, $c$ is the speed of light, $P = e^{-jk_z l}$, and $l$ = the length of the sample. Both $R$ and $P$ are functions of the input frequency $\omega = 2\pi f$, and $\epsilon = \epsilon_0\epsilon_r$.

**Double Sided Material Measurement.**

Four port single source excitation S-parameters must be converted to dual source excitation S-parameters using mixed mode equations [17], [5]

$$S_{11}^{CCorDD} = \frac{1}{2}[(S_{11} + S_{22}) \pm (S_{21} + S_{12})] \tag{49a}$$

$$S_{12}^{CCorDD} = \frac{1}{2}[(S_{13} + S_{24}) \pm (S_{23} + S_{14})] \tag{49b}$$

$$S_{21}^{CCorDD} = \frac{1}{2}[(S_{31} + S_{42}) \pm (S_{32} + S_{41})] \tag{49c}$$

$$S_{22}^{CCorDD} = \frac{1}{2}[(S_{33} + S_{44}) \pm (S_{43} + S_{34})] \tag{49d}$$

where $S_{mn}$ are the measured or simulated system S-parameters. Common mode excitation S-parameters ($S_{mn}^{CC}$) are calculated as the sum of the terms and differential excitation mode S-parameters ($S_{mn}^{DD}$) are calculated as the difference of the first two terms with the latter two terms.

In order to extract the material parameters from the material under test, Thru-Reflection-Line (TRL) calibration is used. In this case, the system under test is a material sample placed in the center of the four port waveguide. Measurements from three standard configurations (i.e., *thru*, *reflection*, and *line*) are required to apply

this calibration to material measurements.

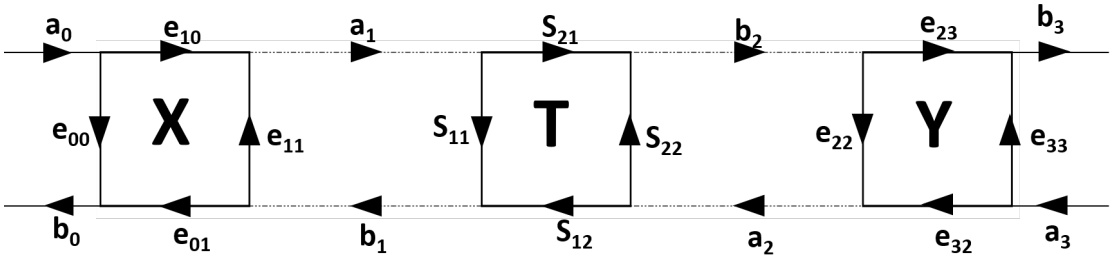


**Figure 9. The error box model for a two-port microwave system.**

TRL calibration uses error boxes to represent the input and output reflection terms as represented in Figure 9. The error boxes $X$ and $Y$ must be characterized in order to extract the true S-parameters of the sample under test [35, 36]. Cascade matrix (T-parameters) are used to represent the system under test

$$T^{mU} = T^X T^U T^Y = \begin{bmatrix} T_{11}^X & T_{12}^X \\ T_{21}^X & T_{22}^X \end{bmatrix} \begin{bmatrix} T_{11}^U & T_{12}^U \\ T_{21}^U & T_{22}^U \end{bmatrix} \begin{bmatrix} T_{11}^Y & T_{12}^Y \\ T_{21}^Y & T_{22}^Y \end{bmatrix} \tag{50}$$

where $T^{mU}$ represents the measured T-parameters, $T^X$ and $T^Y$ represent the input and output reflection T-parameters and $T^U$ represents the T-parameters of the system under test. In this case the system under test is whatever is placed between the two waveguide apertures. The relationship between S-parameters and T-parameters is [14]

$$\begin{bmatrix} T_{11} & T_{12} \\ T_{21} & T_{22} \end{bmatrix} \equiv \frac{1}{S_{21}} \begin{bmatrix} S_{12}S_{21} - S_{11}S_{22} & S_{11} \\ -S_{22} & 1 \end{bmatrix} \tag{51}$$

Solving for the system under test $T^U$ and converting the error box terms to S-

parameters results in

$$T^U = S_{21}^X S_{21}^Y (T^X)^{-1} T^{mU} (T^Y)^{-1} =$$
$$S_{21}^X S_{21}^Y \begin{bmatrix} S_{21}^X S_{12}^X - S_{11}^X S_{22}^X & S_{11}^X \\ -S_{22}^X & 1 \end{bmatrix}^{-1} T^{mU} \begin{bmatrix} S_{21}^Y S_{12}^Y - S_{11}^Y S_{22}^Y & S_{11}^Y \\ -S_{22}^Y & 1 \end{bmatrix}^{-1}. \quad (52)$$

Using this definition, there are eight unknown error terms. Following the TRL calibration procedure and assuming that forward and reverse error terms are identical, only seven of the eight error terms need to be solved in order to calibrate the sample measurements: $S_{21}^X S_{21}^Y$, $S_{21}^X S_{12}^X$, $S_{11}^X$, $S_{22}^X$, $S_{21}^Y S_{12}^Y$, $S_{11}^Y$, and $S_{22}^Y$. The three calibration standards used in TRL calibration allow for each of these terms to be solved. In the *thru* configuration $T^U$ is completely known

$$T^{Thru} = \begin{bmatrix} 1 & 0 \\ 0 & 1 \end{bmatrix}. \quad (53)$$

The line standard represents a phase delay

$$T^{Line} = \begin{bmatrix} e^{-jk_z l} & 0 \\ 0 & e^{jk_z l} \end{bmatrix} \quad (54)$$

where $k_z$ is the $\hat{z}$-directed wavenumber and $l$ is the $\hat{z}$-directed length of the line delay.

The Reflection standard used is a highly reflective load (i.e., an electrical short) which is typically a flat metal plate. All of the $T^{Ref}$ parameters are not required to be known for this standard. It is only required $S_{11} = S_{22}$ for this standard.

Once the S-parameters of the material sample ($S_{mn}^{samp}$) are calculated, the Newton root search method and NRW algorithms are used to extract the forward and reverse relative permittivity and permeability of the material. $S_{11}^{samp}$ and $S_{21}^{samp}$ are used to

calculate the forward $\epsilon_r$ and $\mu_r$ while $S_{22}^{samp}$ and $S_{12}^{samp}$ are used to calculate the reverse $\epsilon_r$ and $\mu_r$.

The double sided Newton root search method calculates the theoretical transmission ($S_{21or12}^{T}$) and reflection ($S_{11or22}^{T}$) S-parameters with

$$S_{11or22}^{T}(\epsilon_r, \mu_r, \omega) = \frac{R(1-P^2)}{1-R^2P^2} \tag{55a}$$

$$S_{21or12}^{T}(\epsilon_r, \mu_r, \omega) = \frac{P(1-R^2)}{1-R^2P^2} \tag{55b}$$

where $R = \frac{Z-Z_0}{Z+Z_0}$, $Z = \omega\mu_0\mu_r/k_z$, $k_z = \sqrt[2]{\omega^2\epsilon\mu - k_c^2}$, $k_c = \pi/a$, $a$ is the width of the rectangular waveguide in meters, $Z_0 = \omega\mu_0/k_{z0}$, $k_{z0} = \sqrt[2]{k_0^2 - k_c^2}$, $k_0 = \omega/c$, $c$ is the speed of light in meters per second, $P = e^{-jk_zl}$, and $l$ = the length of the sample. Both $R$ and $P$ are functions of the input frequency $\omega = 2\pi f$, $\epsilon = \epsilon_0\epsilon_r$, and $\mu = \mu_0\mu_r$.

### 3.4 Transmission Line Metrics

The return loss (RL) coefficient is a measure of the power which is not received by the intended receiver or load. In this research, the RL metric characterizes the input reflection characteristic of a system. RL is calculated as

$$RL = -20log_{10}|\Gamma| \tag{56}$$

where $\Gamma$, or $S_{11}$, characterizes the input impedance mismatch of the model when operating in a specific excitation mode. As the input reflection decreases, the RL value increases. This means that high RL indicates an efficient power coupling and thus a closely match load between the network analyzer and the combination of the excitation pin impedance and dominant mode wave impedance.

Insertion loss (IL) is the transmission coefficient between two points. Here, the two points in question for three port and four port models are the excitation pins or port

and output pins or port. The IL of dual source excitation single sided models cannot be evaluated because input power is only reflected back to the excitation source. IL is a better metric for these models and is calculated as

$$IL = -20log_{10}|T| \tag{57}$$

where $T$, or $S_{21}$, characterizes the power transmission of the waveguide model.

The standing wave ratio (SWR) is a measure of the impedance mismatch in a transmission line. This is calculated with

$$SWR = \frac{1 + |\Gamma|}{1 - |\Gamma|}. \tag{58}$$

A large SWR signifies a large impedance mismatch in the transmission system while a low value signifies a system with a perfectly matched load (i.e., $|\Gamma| = 1$) [31].

# IV. Results

## 4.1 Theoretical Single Mode Operations

Given an interior width of 72.136 mm and an interior height of 16 mm, Table 3 summarizes the all the modes which are excited in the waveguide over the 2 to 12.5 GHz range. Given these cutoff frequencies, from 2.08 to 9.37 GHz only $TE_{m0}$ modes will be excited in the waveguide. Further, by the principle of field superposition, the single mode operation frequency range when operating in common mode excitation is 2.08 to 6.24 GHz due to the suppression of the $TE_{20}$ mode. Alternatively, when operating in differential mode the single mode frequency range is 4.16 to 9.37 GHz due to the suppression of $TE_{10}$, $TE_{30}$, and $TE_{40}$ modes.

**Table 3. Electromagnetic modes excited in designed waveguide. The TE and TM mode cutoff frequency ($f_c$) formulas in Chapter II are used to calculate the which modes are excited and at what frequency for a rectangular waveguide with an interior height of 16 mm and width of 72.136 mm over the 2.08 to 11 GHz frequency range.**

| Mode | Cutoff Frequency (GHz) |
|---|---|
| $TE_{10}$ | 2.08 |
| $TE_{20}$ | 4.16 |
| $TE_{30}$ | 6.24 |
| $TE_{40}$ | 8.31 |
| $TE_{01}$ | 9.37 |
| $TE_{11}$, $TM_{11}$ | 9.60 |
| $TE_{21}$, $TM_{21}$ | 10.25 |
| $TE_{50}$ | 10.39 |

## 4.2 Three Port Model Simulation, Refinement and Analysis

The first model simulated in CST MWS® is a three port waveguide. This is a combination rectangular waveguide launcher and body. The interior width of the waveguide is 72.136 mm with two excitation pins placed 18.034 mm away from the

interior left and right walls. The interior height of the waveguide is set to 16mm and the height of the excitation pins is set to 8 mm. In order to model the 7 mm connectors (PN: 311-07-00-000) as closely as possible, dimensions from the connector's datasheet were used. Appendix C contains the connector datasheet. As a result, the radius of the metal excitation pin is set to 0.635 mm and the radius of the Teflon insulation is set to 2.057 mm. The Teflon insulation also protrudes 5.054 mm into the waveguide. These pin dimensions remain unchanged for all CAD models analyzed in CST MWS®.

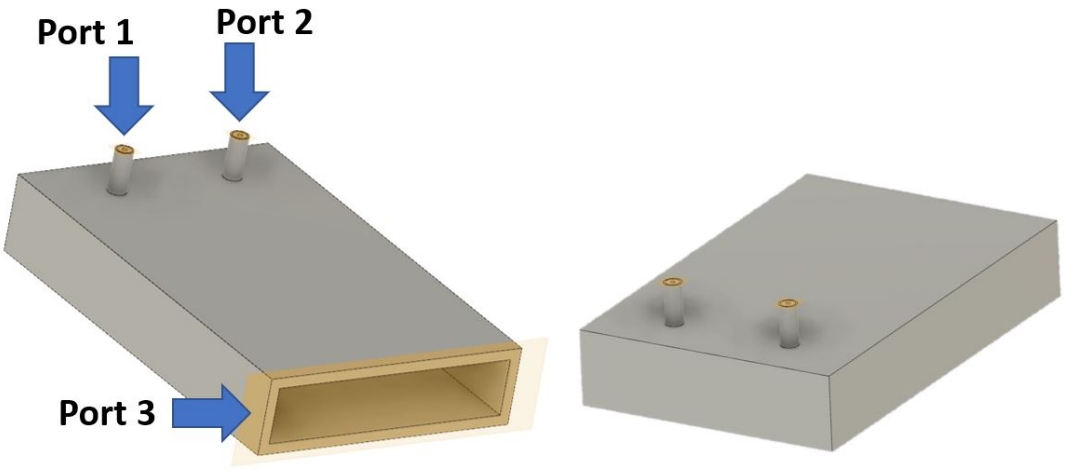


**Figure 10. The three port waveguide model is depicted from the front with simulation ports annotated (left) and from the back (right).**

Using the model depicted in Figure 10, parametric simulations were conducted to determine the optimal pin placement from the back wall of the waveguide which transmitted the most power over the largest frequency range. This was determined by analyzing the power accepted by the aperture port of the waveguide over the simulation frequency range where each excitation pin was driven with a . A 0.67 ns Gaussian pulse with a an average power over the simulation frequency range of 0.5 W was used as the excitation signal. The total simulation time was set to 14 ns in order allow a steady state to be met. It is assumed that all the power which was

transmitted into the waveguide system was either transmitted to the aperture of the waveguide or absorbed by the lossy Teflon material.

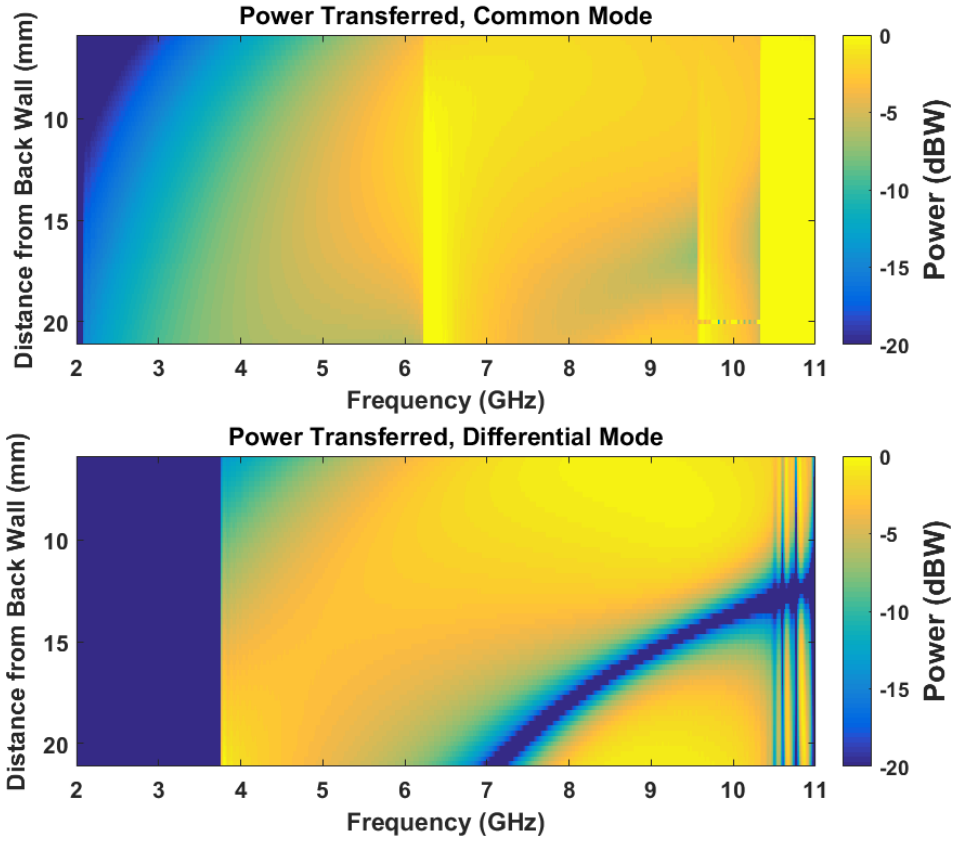


**Figure 11. The power delivered to the aperture of the three port waveguide as a function of pin distances from the back wall is displayed for common (top) and differential (bottom) mode excitation.**

The parametric range simulated was a distance of 21 to 6 mm in 0.25 mm increments for a total of 61 simulations. From these simulations the power accepted by the aperture (port 3) as a function of frequency was analyzed to determined pin placement efficiency. Figure 11 shows the power delivered to Port 3 as a unction of distance ($d$) and frequency in common and differential excitation mode. It was found that as the pins were moved closer to the back wall of the waveguide, in differential excitation mode a null in the power delivered to Port 3 develops. Moving the pins too close to the back wall adversely impacts the total power delivered to the aperture

at low frequencies in both common and differential modes. The pin distance which provides the most power to the aperture over the largest bandwidth is 12 mm. At this distance and over the single mode operation frequency range Port 3 receives on average 0.227 W in common mode and 0.474 W in differential mode. This corresponds to a quarter wavelength frequency of 6.25 GHz. The median of the single mode operation frequency range in differential mode is 7.2 GHz which has a quarter wavelength of 10.4 mm. Although this pin distance transported an average of 0.623 W in differential mode over the single mode frequency range to the aperture, the power delivered as a function of frequency was less stable compared to that of the chosen distance of 12 mm.

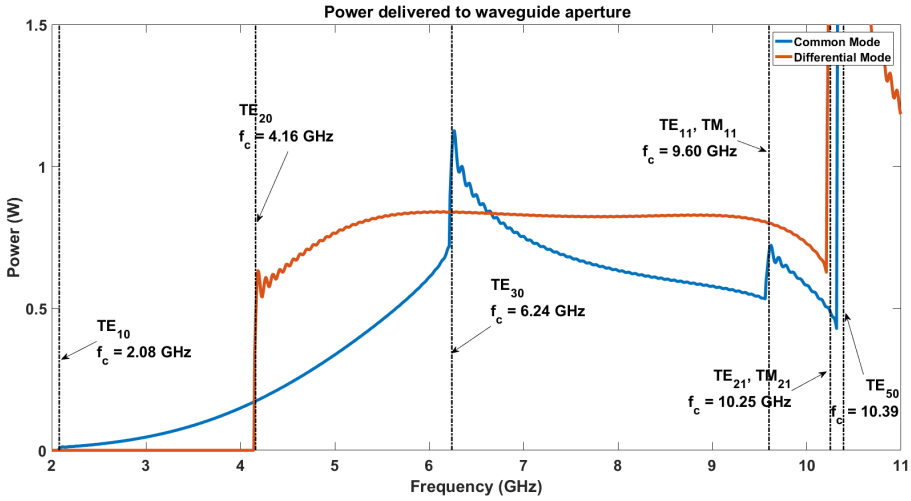


**Figure 12. The total power delivered to the aperture of a dual source rectangular waveguide when operating in common or differential excitation modes.**

The total power delivered to the aperture of the launchers is shown in Figure 12 for both operation modes. Annotated on the plot are the cut off frequencies at the points which seem to experience a significant change in the power delivered to the aperture. Only six of the ten mode cut-off frequencies are annotated because not all ten modes excited in the 2 to 11 GHz range substantially impact the total

power delivered to the aperture. From the plot, it is apparent that the single mode operational frequency range is larger when operating in differential mode rather than common mode. Further, the shape of the power delivered with respect to frequency is better when operating in differential mode as evidenced by the flat response from 5.5 to 9.25 GHz. An issue prevalent in both power curves is a rippling which disrupts the curves minimally. This rippling is worse in the differential operation single mode frequency range. Over this range the mean power delivered is 0.827 W (-0.8276 dBW) with a variance of $2.19\times10^{-4}$. If a -2 dBW insertion loss is used as a standard for the waveguide, the waveguide can operate from 4.4 to 10.2 GHz with $TE_{20}$ as the single mode. This leads to a mean power delivered of 0.804 W (-0.95 dBW) and a variance of 0.0023 over this frequency range. This indicates that the waveguide operates efficiently in differential mode from 5.5 to 9.25 GHz using $TE_{20}$ as the single electromagnetic mode excited.

### 4.3 Power Coupling Analysis

With the effect of the distance to the back wall investigated and the design set, the power contained in each electromagnetic mode is analyzed. In Figure 13 the modes not suppressed in a single source waveguide are compared to those not suppressed in a three port waveguide with the same dimensions excited in common or differential mode. The single source, traditional waveguide does not use field superposition to suppress electromagnetic modes. This means that the modes which are suppressed in the single source, traditional waveguide are due to the placement of the excitation pin. As a result, $TE_{10}$, $TE_{30}$, and $TE_{50}$ modes efficiently couple into the system due to the shape of the $E_y$ fields these modes excite. Because the single excitation pin in the traditional waveguide is placed at a null of the $E_y$ fields excited by $TE_{20}$ and $TE_{40}$ modes these modes do not couple into the system efficiently. It can be concluded

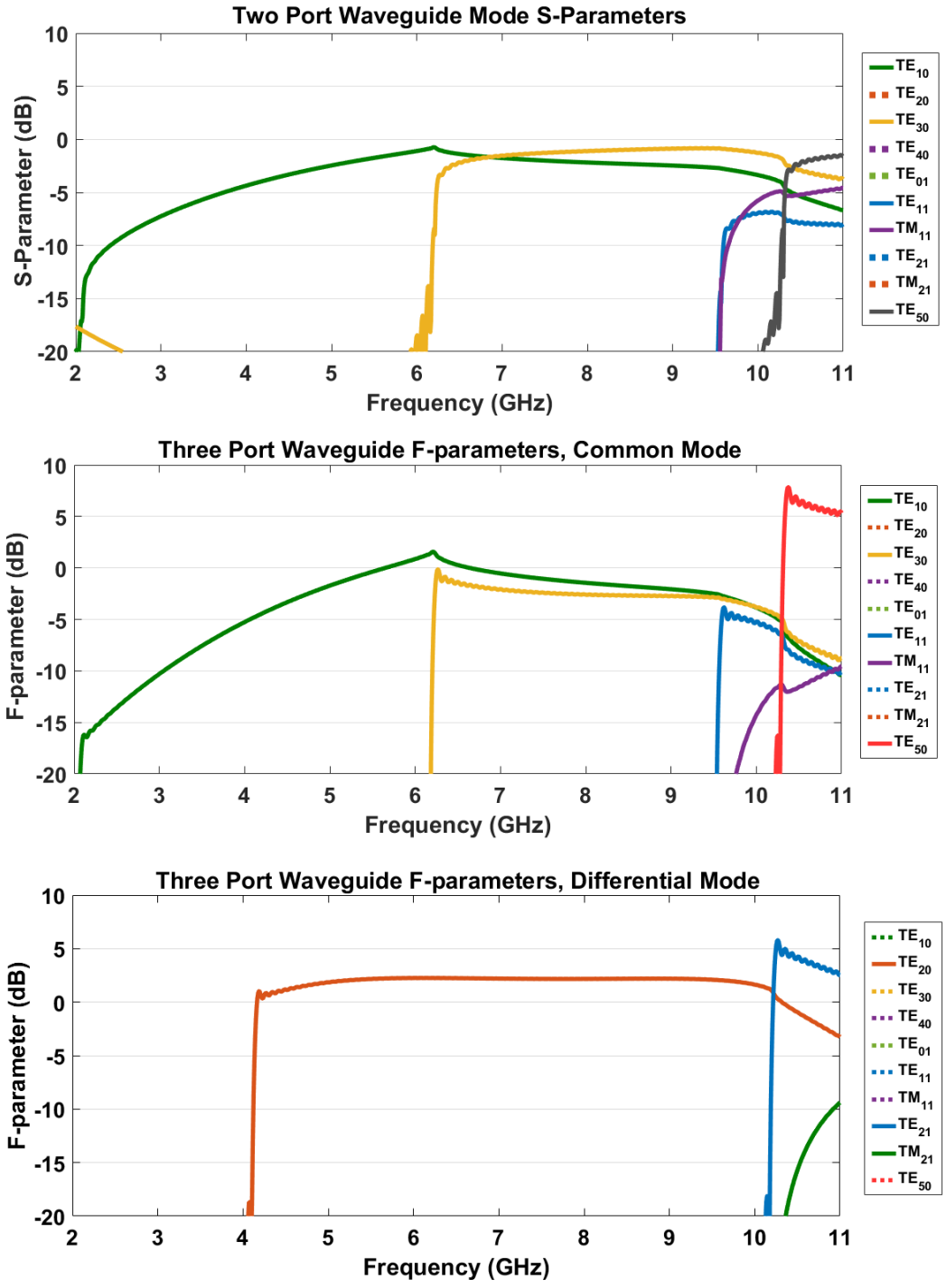


**Figure 13.** A visual comparison of the amplitude of each TE and TM mode excited in a two or three port waveguide is provided. A single source excitation two port waveguide (top) excites different modes from the dual source excitation waveguides with the same interior dimensions excited in common mode (middle) or differential mode (bottom) [23].

then that the placement of the excitation pin(s) has a significant impact on the modes which can couple into a waveguide system. The middle and bottom plots in Figure 13 show that field superposition efficiently suppresses the $TE_{20}$ mode in common mode excitation and both $TE_{10}$ and $TE_{30}$ modes in differential mode excitation.

Before moving on to two and four port models, a characterization of the input and output power coupling capability provides insight into the system efficiency. The two and four port models are electrically closed systems. Thus, power can only couple into or out of the system in specific ways: from the input source to the excitation pin(s) (i.e., input), from one excitation pin to the other (i.e., crosstalk), and from the non-excitation pins to the receiver (i.e., output). Power can be absorbed by lossy materials like copper and Teflon. Both copper and Teflon materials were simulated with low losses in CST, minimizing the amount of loss due to these materials. Simulations analyzing the power coupling capability of the designed waveguide use the three port model in Figure 10 with minor modifications detailed when appropriate.

In order to isolate the input reflection and determine the input coupling and crosstalk, a single pin was excited. The signal received by the unused excitation pin and the waveguide aperture were collected. The reflection percentage was determined by taking the ratio of power reflected by the excitation pin and incident signal power. The cross talk and transmission percentages were calculated similarly.

The time-based signals in Figure 14 show that a significant portion of the incident signal is reflected back to the source. On the other hand, the amount signal which is lost to excitation pin crosstalk is small. Finally, signal received by the aperture is divided into the three $TE_{m0}$ modes excited over 2 - 11 GHz. Power in the other seven modes was negligible.

The output coupling capability was analyzed by using the waveguide aperture as the excitation source. The signal from the aperture is a single mode signal (either

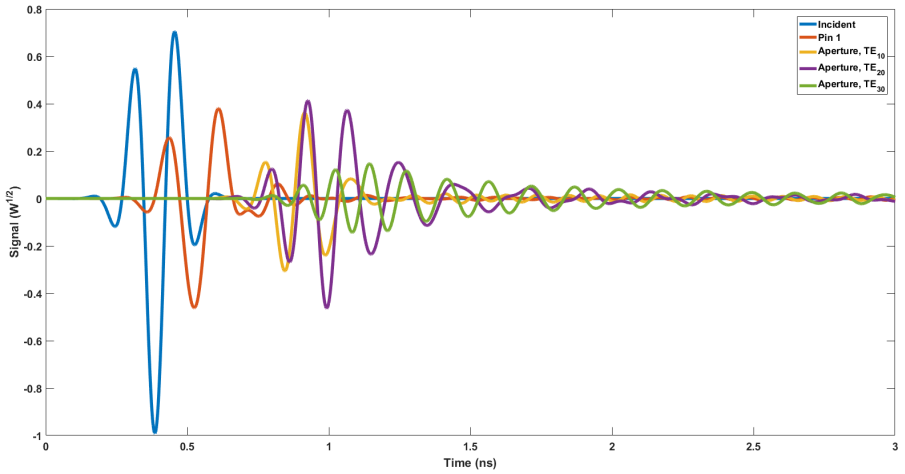


**Figure 14. The time domain signals are plotted for the three port model when only pin 1 is excited.**

$TE_{10}$ or $TE_{20}$) and simulated over the single mode frequency range for common ($f$ = 2.08 - 6.24 GHz) or differential ($f$ = 4.16 - 10.25 GHz) excitation.

In Figure 15, the incident signal, signals received by pins 1 and 2, and the reflection signal (i.e., the aperture signal) are plotted for $TE_{10}$ and $TE_{20}$ single mode excitation. This simulates operation with either $TE_{10}$ or $TE_{20}$ single mode excitation. In the single sided and double sided configurations, power which is not coupled out of the system continues to reflect back and forth in the waveguide until most of the power is removed. The system is more efficient in coupling with $TE_{20}$ mode signals rather than $TE_{10}$. This is due to the placement of the excitation pins at the points where the $E_y$ field component of the $TE_{20}$ mode are maximum.

Numerical results in Table 4 provide further insight into how the waveguide couples power into and out of the system. A significant amount of power is reflected back to the source by the waveguide when operating with a single source. This is due to an impedance mismatch when the input signal transitions from the simulation port (or network analyzer cable) to the interior of the rectangular waveguide [11, 33]. This is

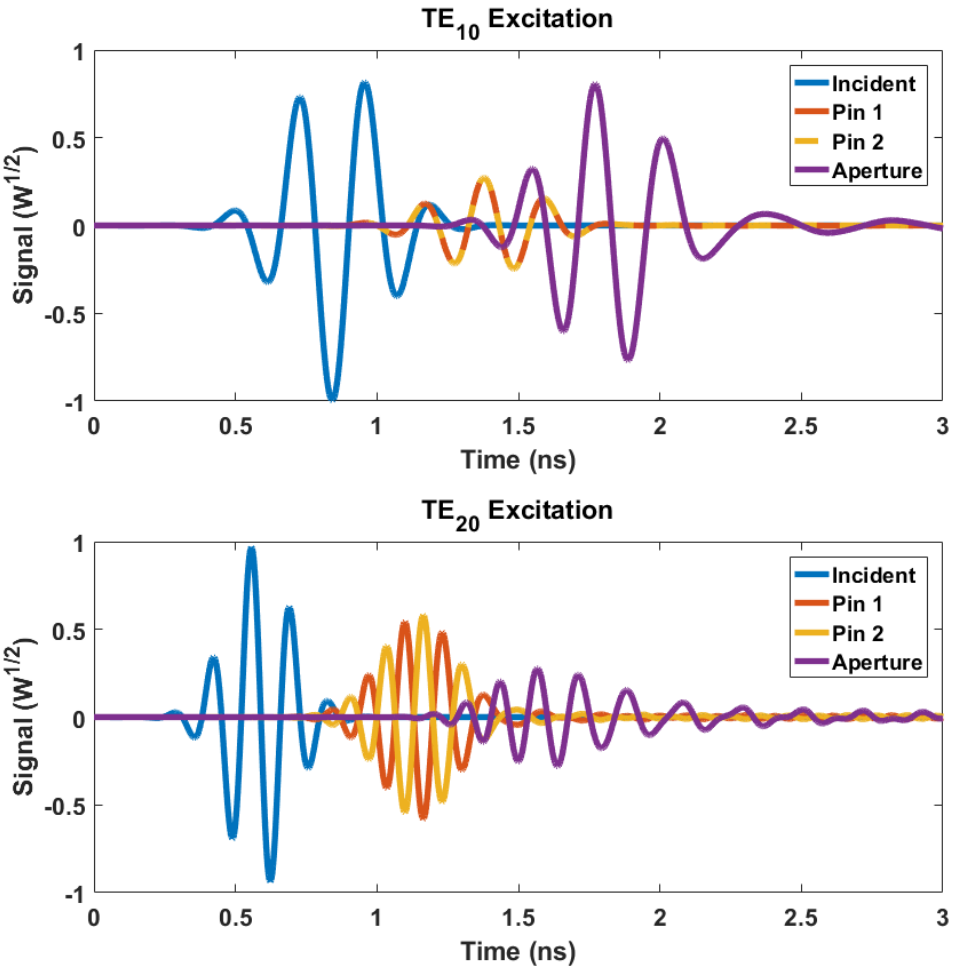


**Figure 15. The time domain signals are plotted for the three port model when the aperture excites only $TE_{10}$ or $TE_{20}$ modes.**

**Table 4. The power coupling capability of the waveguide for input signals (top) and output signals (bottom) is displayed. Results are based on the average signal reflected or transmitted over the stated frequency range. The output percentages are the amount of the incident signal which couples out of the waveguide.**

| **Input (f = 2 - 11 GHz)** | |
|---|---|
| **Metric** | **Output (%)** |
| Reflection | 29.6 |
| Crosstalk | 0.9 |
| Transmission | 69.5 |
| **Output (single mode)** | |
| **Dominant Mode** | **Power Coupled Out (%)** |
| $TE_{10}$ (f = 2.08 - 6.24 GHz) | 16.77 |
| $TE_{20}$ (f = 4.16 - 10.25 GHz) | 82.52 |

an issue for which many solutions have been proposed as reviewed in Chapter I.

Of the 69.5% of power which does couple into the system, much of that power reflects back and forth in waveguide before coupling out of the system. When operating in common excitation mode, 16.77% of the power in $TE_{10}$ couples out of the system each time a pulse reaches the output pins. Alternatively, 82.52% of the power in $TE_{20}$ couples out of the system each time a pulse reaches the output pins. The power reflects back and forth until virtually all of it is removed from the waveguide. When operating in single sided mode, all the power which couple into the system is received by the same two excitation pins. In the double-sided configuration, the power which couples into the system is first received by the non-excitation pins, and a portion of the power is reflected back to the excitation pins and so on. The power in the $TE_{10}$ mode will reflect within the waveguide for longer than that in the $TE_{20}$ mode.

Figure 16 shows the transmission coefficients for single mode output coupling as a function of frequency. This plot indicates there are three distinct frequencies for which $TE_{20}$ inefficiently couples out of the waveguide: 9.0 GHz, 9.6 GHz, and 10.1 GHz. The latter two frequencies roughly correspond to the cutoff frequencies for

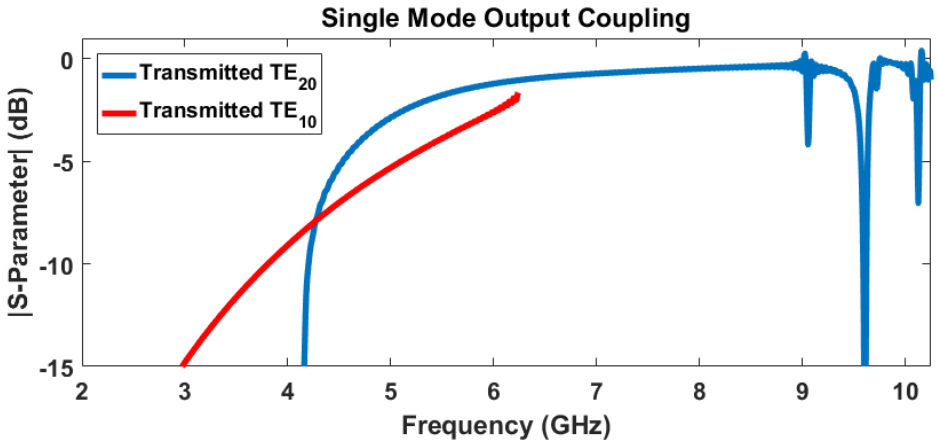


**Figure 16. The singe mode transmission coefficients are displayed for $TE_{10}$ and $TE_{20}$. The frequency over which the modes are plotted corresponds to the single mode frequency range for common ($TE_{10}$ and $f = 2.08$ to 6.24 GHz) and differential ($TE_{20}$ and $f = 4.16$ to 10.25 GHz) excitation.**

$TE_{11}$, $TM_{11}$ and $TE_{21}$, $TM_{21}$ modes respectively. The excitation of these degenerate modes may cause the output power couple inefficiency.

### 4.4 Single Sided Simulation and Measurement

In order to design a four port model which could be manufactured and test, certain changes were made to the original three port model. In order to allow the model to be manufactured with wire EDM, a removable back plate was designed which would attach to the waveguide with bolts. Because the 7 mm connectors selected for this research contained a 1.25 in (or 31.75 mm) diameter flange of their own, the excitation pins have to be moved away from the back plate 8 mm. To compensate for this movement, the removable back plate was designed to include a block of metal which would artificially move the back plate 8 mm closer to the excitation pins. In order to ensure that the excitation pins maintained the 8 mm height inside the waveguide, the bottom thickness of the waveguide was adjusted. The total height of 7 mm connector excitation pins is 0.708 in (or 17.98 mm). This required that the bottom thickness of

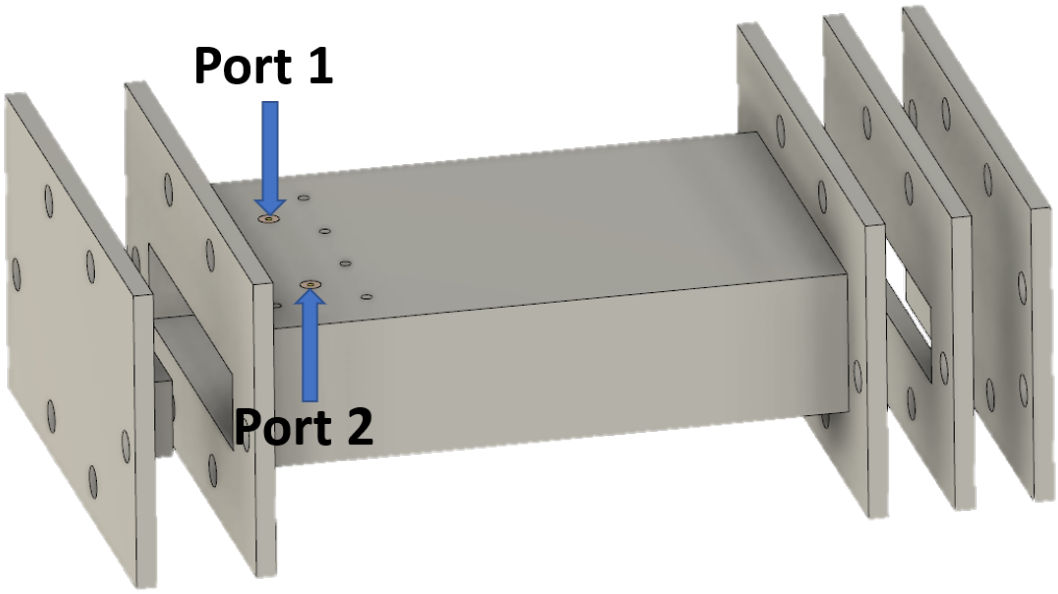


**Figure 17. An exploded view of the two port waveguide model used for production and simulation is shown with a sample holder placed between the aperture of the waveguide and a flat PEC plate.**

the waveguide be roughly 10 mm. In order to extract material properties using the TRL calibration procedure, sample holders and a flat plate were also manufactured. The original drawing files used for the physical models are in Appendix C. The final two port model is depicted in Figure 17 which includes the aforementioned CAD model alterations.

The four S-parameters collected from the waveguide were analyzed in single source excitation and dual source excitation modes. Because single source excitation S-parameters can be converted to dual source excitation S-parameters with mixed mode equations in Chapter III, the same data sets are used for both calibration and material parameter extraction.

**Single Source Excitation Measurements.**

Single source excitation activates one pin at a time. As a result, the reflection S-parameter is the only S-parameter used for analysis. Reflection coefficients were generated with the transient domain solver in CST MWS® in order to validate physical model measurements. Physical measurements were conducted with calibrated network analyzer using a 2.3 ms sweep of the frequency range of interest. In Figure 18 the measured and simulated data are plotted together for two epoxy resin samples of different thicknesses. Calibration measurements and simulations were conducted with two sample holders of different thicknesses (4 mm, 9.5 mm) and a flat plate. This was done in order to move the electrical short to different distances away from the aperture of the waveguide.

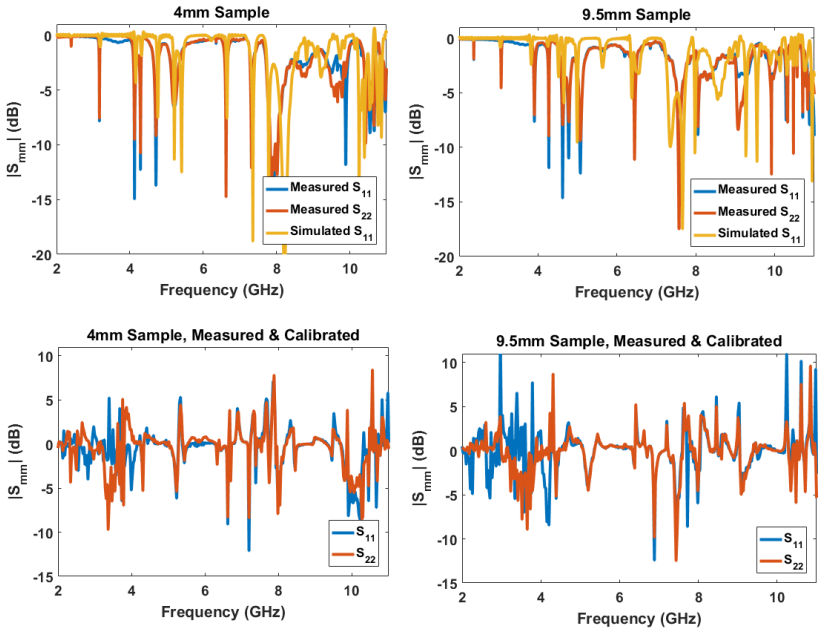


**Figure 18. Measured, simulated, and calibrated sample measurement data.**

The two samples measured are 3D printed epoxy resin blocks inserted into the sample holders. The simulation sample used was a lossless material with $\epsilon_r = 4$ while

the material samples are assumed to have a $\epsilon_r = 3.2$ [40]. The extracted $\epsilon_r$ plotted in Figure 19 show that both the simulation and measurement data have significant flaws when used in extracting an accurate relative permittivity. A deeper look into

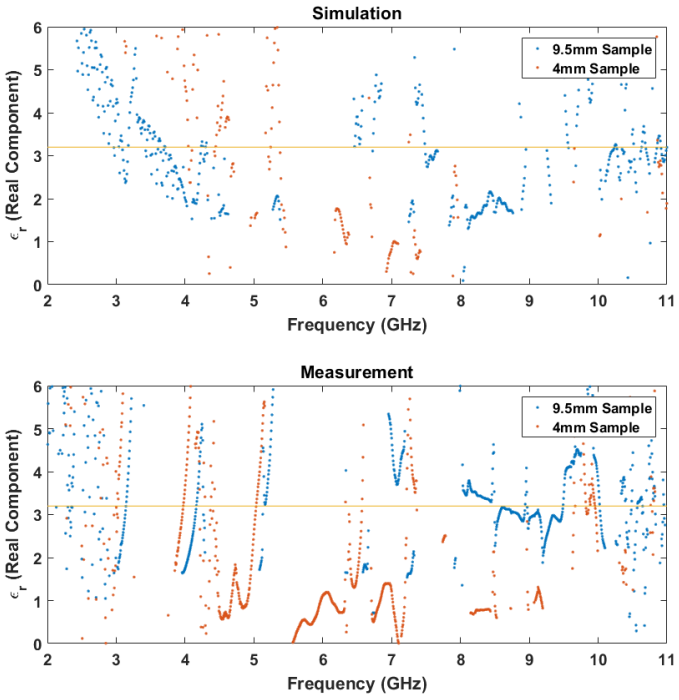


**Figure 19. The real component of $\epsilon_r$ extracted with Newton's root search method is plotted for single source excitation for 4mm and 9.5mm epoxy resin samples.**

the calibration data explains why the parameter extraction failed. The results of the calibration applied to the sample measurement data in Figure 18 are not physically realistic. The reflection coefficient of a simple dielectric sample like the epoxy resin should never be greater than one. This would imply that the signal received from the sample is greater than the signal incident on the sample. Another point of concern is the rapid oscillation of the calibrated $S_{mm}$ with respect to frequency.

The offset short calibration method uses a theoretical reflection coefficient

$$\Gamma^{thy} = -e^{j2l_s k_{z0}} \tag{59}$$

where $\Gamma^{thy}$ is the theoretical reflection coefficient at the aperture of the waveguide where $z = 0$, $l_s$ is the distance of the short from the aperture of the waveguide, and $k_{z0}$ is the $\hat{z}$ directed wavenumber in free space of the dominant $TE_{10}$ mode. Because this calibration method depends on the phase shift induced by the offset shorts, the standards used must not be multiples of half the wavelength of the operational frequencies (i.e. $l/(0.5 + n)$) . This means that the 9.5mm offset short is ineffective for waves with frequencies of 15.75 GHz, 47.24 GHz, and so on. In the same way, the 4 mm offset short is ineffective for waves with frequencies of 37.5 GHz, 112.5 GHz, and so on [35]. These ineffective frequencies are all well above the range of interest in this research.

Based on this, it is apparent that the three-term error model used in the calibration method is not suitable for this system. This is because there is a source of error which this calibration scheme does not model properly as shown in Figure 18. An accurate calibration method produces data which can be used to extract $\epsilon_r$. Further simulation is required to determine why all power transmitted into the single-sided waveguide is not transmitted out as seen in Figure 18. Basic theory indicates that —$S_{11}$— and —$S_{22}$— should be equal to 1.

**Dual Source Excitation.**

Single source data is converted to dual source data with the use of Equation (49a). This is accomplished with both simulated and measured data. The dual source simulation and measurement data sets now do not agree with each other. Figure 20 shows this for both common and differential excitation modes. The measured reflection coefficients show significant attenuation where the simulation data shows there should be none. The same calibration algorithm was applied to the simulation and measurement data with similar results as single source excitation calibrated data.

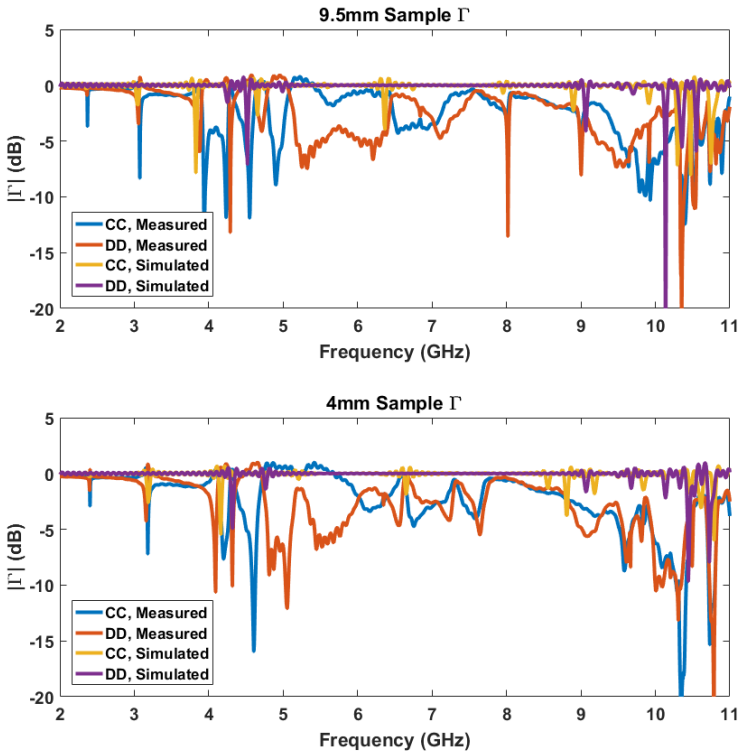


**Figure 20. Dual source excitation reflection data measured and simulated are presented for two epoxy resin samples.**

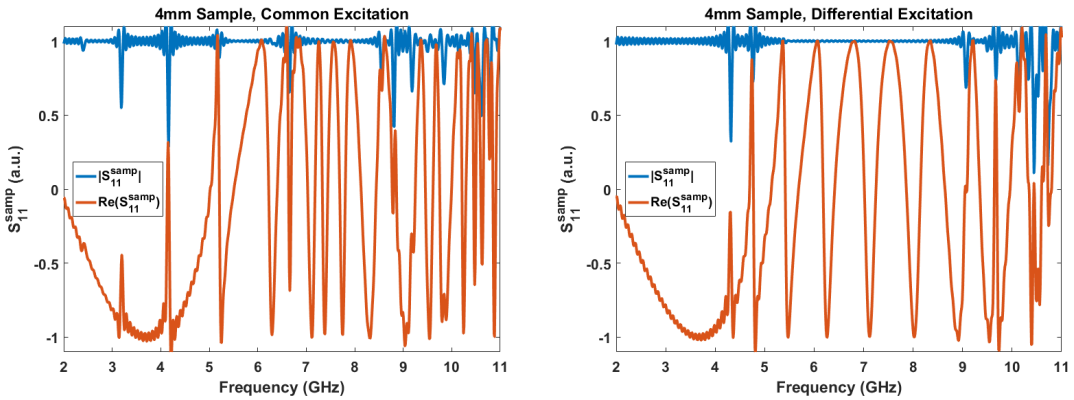


**Figure 21. The magnitude and real component of the simulation data for the dual source single sided model operated in both common and differential excitation modes.**

Inconclusive results were generated by the Newton root search method when applied to the calibrated sample data. The reflection data in Figure 20 seems to indicate that $\epsilon_r$ can be extracted because the magnitude of the reflection coefficient oscillates about 1. In reality, the real and imaginary components of that data are not suitable for material parameter extraction. The comparison plots in Figure 21 show that the real component of the data (and also the imaginary component which is not shown) oscillates wildly. In reality, the theoretical reflection coefficient does not oscillate in this manner. This is why $\epsilon_r$ extraction was inconclusive with this data as well. While single-sided waveguide simulations and measurements were inconclusive in extracting $\epsilon_r$ from nonmagnetic dielectric samples, further research should be conducted in single-sided waveguide data analysis.

### 4.5 Double-Sided Simulation and Measurement

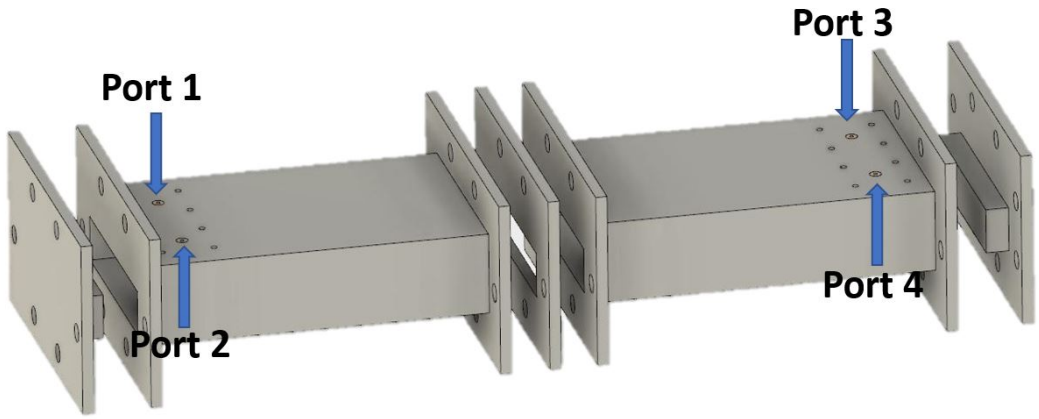


**Figure 22. An exploded view of the four port waveguide model used for production and simulation is shown with a sample holder placed between the apertures of the two end of the waveguide and the ports annotated.**

Double-sided measurements and simulations were conducted with the waveguide in the configuration depicted in Figure 22. Simulations were conducted in single

source excitation with the transient domain CST MWS® solver. Physical model measurements were taken with a two port network analyzer and converted to dual source excitation S-parameters with the mixed mode equations presented in Equation (49).

***Thru* Measurement and Simulation.**

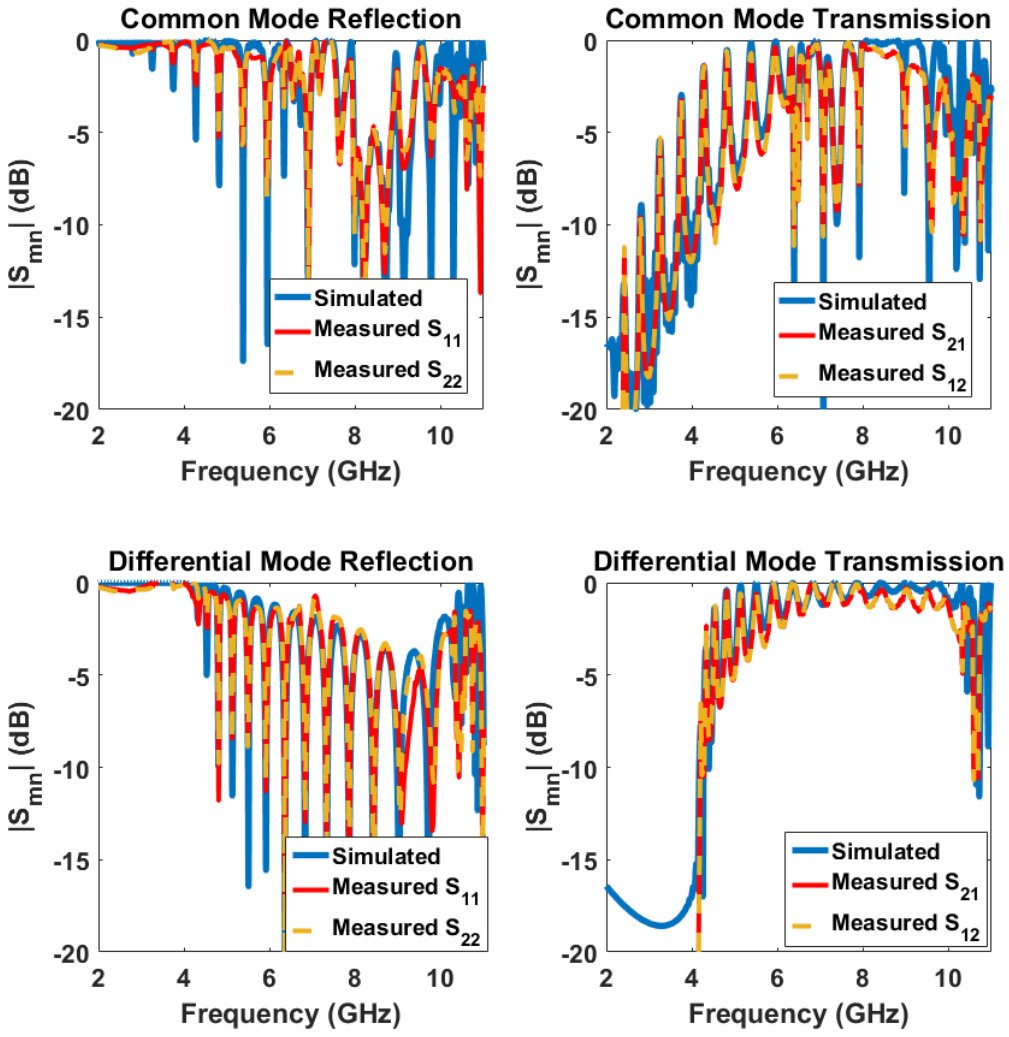


**Figure 23. Common (top) and differential (bottom) mode simultaneous excitation S-parameters plotted for both simulated and measured data.**

The *thru* configuration characterizes the waveguide's ability to transport power. In this configuration, the waveguide apertures are connected directly together. The CAD model ports were defined so that the reference plane was at the exterior of the waveguide. Physical measurements mirrored this by calibrating the network analyzer to the end of the cables.

The simulation and measurement data show an overall level of agreement in Figure 23, but they both diverge from the three port launcher model in Figure 12. Use of the transient domain solver in CST caused the low frequency ringing apparent in the common mode S-parameters from 2 to 5 GHz. This phenomenon is present in the differential mode S-parameters but less pronounced due to the dominant $TE_{20}$ excitation at 4.16 GHz. The ringing can be mitigated with longer simulation times. Despite minor inconsistencies, the measured data validates the simulation data. The measured and simulated S-parameters depart from the expected frequency response in Figure 12. This is likely due to the power which reflects back and forth in the waveguide.

The time and frequency domain signals in Figure 24 support the notion that pulse reflection in the body of the waveguide contribute to the unexpected results in Figure 23. The *ref* and *thru* configurations have two distinct time-based signal characteristics which result in different frequency-based power transmitted in each configuration. Each of the configurations was simulated with identical excitation signals. Both time domain plots show portions of the excitation signal reflected back to the source. This is the first pulse seen from $t < 1$ ns. In the *thru* configuration, after the signal couples into the system, some of the signal is received by the output pins but a portion of the signal is reflected back to the excitation pins ($t > 2$ ns). This second pulse received by the excitation pins is likely responsible for the shape of the frequency domain power transmission. In the sample configuration both the

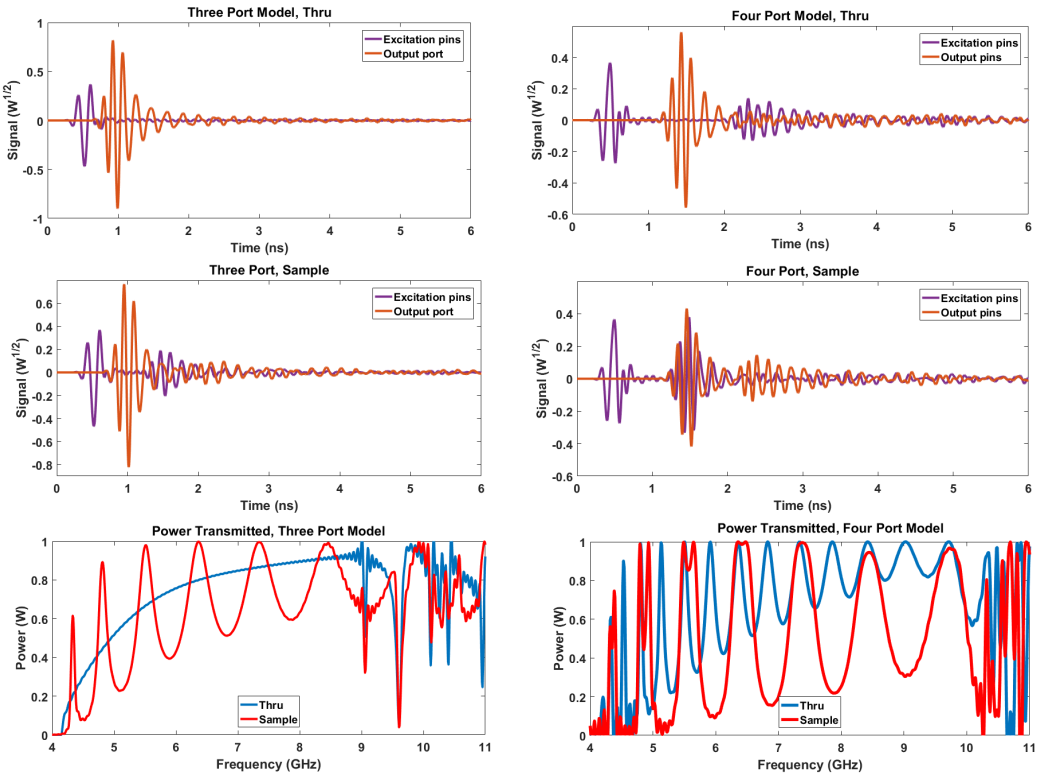


**Figure 24. Time and frequency domain plots show the impact that waves reflecting back and forth in the three port model and four port waveguide. The plots on the left show the thru (top left) and sample (mid left) time domain signals which transmit the total power (bottom left) to the waveguide aperture. The plots on the right show the thru (top right) and sample (mid right) time domain signals which transmit the total power (bottom right) to the output pins.**

excitation pins and output pins receive a signal pulse almost simultaneously. This is physically intuitive due to the nature of plane wave reflection and transmission at material boundaries [3]. The second pulse received by the output pins (t $>$ 2 ns). This means that the power contained in the time-domain pulses which are reflected back and forth in the waveguide are the cause of the unexpected rippling features in Figure 23. This can be mitigated with an improved waveguide-to-coax transition which would minimize the power reflected in the waveguide.

**Material Measurement.**

The *thru* configuration results show the impact of the inefficient output power coupling of the designed waveguide. Despite this, material measurement can be conducted with the double-sided waveguide. Electromagnetic material measurement with the four port waveguide requires a TRL calibration in order to calculate the forward and reverse transmission and reflection coefficients. Simulation and measurement TRL models used a flat metal plate as the reflection standard and an empty 4 mm sample holder as the line standard. The same two physical samples used in single sided-measurements were used again in double-sided measurements along with the same 4 mm epoxy sample in CST with $\epsilon_r = 4$.

The calibrated measured and simulated dual-source S-parameters indicate that the measurement data is unsuitable for material parameter extraction. This is due to the familiar unrealistic and unstable set of transmission and reflection coefficients seen in the calibrated single side S-parameters in Figure 18. On the other hand, the calibrated simulation S-parameters show regions in which material parameter extraction is possible. Most notably is the 5.5 - 10 GHz range in differential mode excitation. Material parameter extraction conducted on the calibrated simulation data with both Newton's method and the NRW method in Figure 25 show that

material parameter extraction can be conducted with this system.

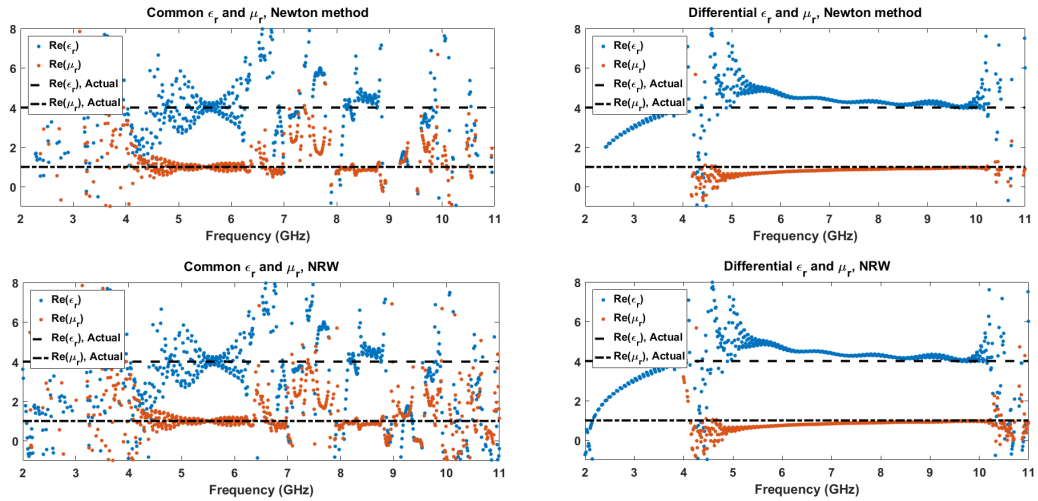


**Figure 25. The extracted material parameters with both the Newton method and the NRW algorithm are plotted for a dual source double sided waveguide.**

Minor differences exist in the regions in which both methods successfully extracted the relative permittivity of the dielectric sample. Over the 5.5 to 10 GHz range, the real part of the $\epsilon_r$ extracted by both methods differed by $4.06\times\ 10^{-13}$. With a real $\epsilon_r$ of 4, both results were on average within 8.78% of the actual answer. While neither method was more accurate in the region of interest, the NRW method produced results in only 1.70% of the time that the Newton method required to produce results. This is due to the iterative nature of the Newton method. While only two function calls were required to process the calibrated data with the NRW method, the Newton method used 75,366 function calls, or iterations, to process 1,001 data points. The maximum number of iterations was set to 1,000 and the tolerance was set to -140 dB. The number of function calls used by the Newton method to produce results is a function of the maximum number of iterations allowed, the accuracy of the initial guess and the stability of the calibrated data. It should be noted that the originally determined single mode operation range of 4.16 to 10.25 GHz encompasses the range

for which material parameters could be extracted.

### 4.6 Transmission Line Metrics

Metrics are calculated with data collected when the models are operated in differential mode due to the superior single mode operation bandwidth. Not every metric is suitable for every model. The single-sided two port models are not intended to transmit power. Thus the RL and SWR metrics are not presented for these models.

**Table 5. Transmission line metrics for the three port models operated in differential excitation mode.**

| **Model** | **RL (dB)** | **IL (dB)** | **\|SWR\|** |
|---|---|---|---|
| Thru | 4.19 | 9.15 | 5.17 |
| Sample (4mm) | 3.55 | 11.15 | 15.15 |
| Aperture Excitation,$TE_{20}$ | 14.66 | 3.34 | 2.16 |

The data in Table 5 provide baseline metrics by which the two port models and four port models are compared. The aperture port is a perfect measure of the power coupled into the system with the excitation pins (as in the *thru* and sample configurations) or a perfect source of single mode signals over an arbitrary frequency range (as in the aperture excitation configuration). The impedance mismatch of the waveguide pins is quantified in *thru* and aperture excitation model SWR values. The thru SWR quantified the input impedance mismatch while the aperture excitation SWR quantified the output impedance mismatch over the differential excitation single mode frequency range. The coax-to-waveguide impedance mismatch drives the *thru* SWR value while the electric field coupling impedance mismatch drives the aperture excitation SWR value. The sample model SWR provides a baseline for double sided sample model SWR. The RL and IL results in the *thru* configuration confirm the power coupling analysis conducted in Table 4.

The IL values in Table 6 further show the difference between the simulated and

**Table 6. Reflection loss for two port models operated in differential excitation mode.**

| Model | Simulation RL (dB) | Measurement RL (dB) |
|---|---|---|
| $l$ = 0mm | 0.08 | 5.87 |
| $l$ = 4mm | 0.22 | 4.55 |
| $l$ = 9.52mm | 0.11 | 5.86 |
| sample, 4mm | 0.12 | 6.28 |
| sample, 9.5mm | 0.28 | 5.71 |

measured dual source single sided waveguide data. In this configuration it is assumed that all the incident power is reflected back to the source by either the excitation pin impedance mismatch or by the PEC plate in the waveguide. A RL $\neq$ 0 implies that not all the power delivered to the system is reflected back to the source. In the simulation domain the average RL for all five models is 0.162 dB which means that 98.2% of the incident power is reflected back to the source. The missing 1.8% of the power incident power may either have been consumed by the lossy Teflon material or simply not have coupled out of the system (i.e., steady state was never achieved).

The measurement data has an average RL of 5.65 dB for the five models which means that 52.1% of the incident power is reflected back to the network analyzer. This significant departure from the simulation data may be due to physical gaps between the 7 mm flange plates and the waveguide or from gaps between the back and front PEC plates.

**Table 7. Transmission line metrics for the four port models operated in differential excitation mode.**

| | Simulation | | | Measurement | | |
|---|---|---|---|---|---|---|
| Model | RL (dB) | IL (dB) | \|SWR\| | RL (dB) | IL (dB) | \| SWR\| |
| Thru | 8.04 | 2.73 | 2.27* | 8.83 | 3.48 | 5.9 |
| Line | 8.18 | 2.17 | 11.01* | 9.29 | 3.46 | 4.89 |
| Sample, 4mm | 5.16 | 5.37 | 16.46 | 9.69 | 5.36 | 5.44 |
| * = negative values | | | | | | |

The transmission line metrics from the four port models in Table 7 in addition to the three port model metrics in Table 5 quantify the performance of the double sided waveguide when operated in differential excitation mode. Between the simulation and measured models RL increased an average of 2.14 dB and IL increased 0.68 dB. The trend of higher RL and IL values calculated from the measurement data when compared to the simulation data can be attributed to physical sources such as the 7 mm connectors or network analyzer cable connections. The four port model simulation RL and SWR are comparable to that of the three port model RL and SWR. The difference in these two metrics between the three and four-port models further quantifies the impact of excitation pins. By receiving power with two excitation pins rather than the aperture port results in a RL increase of 1.61 dB and a SWR increase of 1.31 or 8.65%.

### 4.7 Error Sources

Error analysis can be conducted on measurement data and simulation data independently. This is because the sources of error are fundamentally different for the data collected or generated by the different methods employed. Measurement data is the most susceptible to error as evidenced by the inconclusive double sided material measurement results. The error which influenced the measurement data takes two forms: systemic and random. Systemic errors include physical gaps in the waveguide where there should be none, improper application of calibration methods, and poorly sized material samples. These error sources are controlled through good practices like appropriate manufacturing tolerances, proper calibration methods standards and algorithms, and careful sample preparation. Random error in measurement data from the two port network analyzer is mitigated by allowing extended sweep times, keeping the network analyzer cables in roughly the same position, and averaging multiple

results together.

Error in the results from numerical analysis had specific tolerance or accuracy levels. The Newton root search method used a set numerical accuracy to halt iterations of -140 dB. CST MWS® simulations were set to a -50 dB accuracy. The two CST MWS® solvers use different CEM meshing algorithms to set points to solve Maxwell's equations. In order to improve the accuracy of the model mesh, a maximum point spacing of $\lambda_{min}/10$ or 2.7 mm was set. Further, Adaptive Mesh Refinement was implemented in all simulations.

# V. Conclusion

In the first phase of this research, a dual source excitation rectangular waveguide launcher was designed, simulated, manufactured, tested, and analyzed. Starting with a hypothesis as to the implication of a dual source excitation design, a launcher was designed with two excitation pins symmetrically placed in a rectangular waveguide. The result of the pin placement and the superposition of the excited $E_y$ fields for each $\mathrm{TE}_{m0}$ mode was an effective suppression of $E_y$ fields for certain modes. Driving the dual source excitation launcher with signals in either a Common or Differential mode determines which $E_y$ fields are suppressed: common mode excitation suppresses the $E_y$ fields of even $\mathrm{TE}_{m0}$ modes while differential excitation mode suppresses odd $\mathrm{TE}_{m0}$ modes. Regardless of the excitation mode, $\mathrm{TE}_{40}$ is not excited due to the placement of the excitation pins at the nulls of the $E_y$ field.

It is the shape of the standing $E_y$ waves along with the physical placement of the pins which causes power to poorly couple into and out of the system. Traditional waveguides contain a single excitation pin centered in the middle of the waveguide's XY plane because this corresponds to the maximum point of the $E_y$ field excited in the $\mathrm{TE}_{10}$ mode. The operational frequency for these waveguides is set such that only the $\mathrm{TE}_{10}$ mode is excited. By placing pins away from the location of the maximum of the $E_y$ field and operating outside of the single mode frequency range, the system begins to experience less and less efficient operations. Power coupling structures can be included in the waveguide which will assist in coupling power into and out of the system and improve overall performance.

In the second phase of the research, the dimensions of the three port launcher model were used to design both a single sided two port model and a physical model. The physical model was manufactured and tested in order to validate the simulation results. Material measurement results were inconclusive for both the physical model

and CAD model data when operated with either a single source or a dual source.

The third phase of the research involved a four-port CAD and physical model. The physical model *thru* measurements showed an initial agreement with the simulation data but the TRL calibration resulted in unsuitable data for the NRW or Newton material parameter extraction methods. The four-port calibrated simulation data extracted marginally accurate material parameters over the 5.5 to 10 GHz range.

The results of this research is the starting point for further dual source excitation rectangular waveguide design. The success in extracting the relative permittivity and permeability of the sample simulation proved that the dual-source excitation design can be used in material measurement. As shown through plots of simulation and measurement data, more design and research work must go into addressing the impedance mismatch in the coax-to-waveguide transition. The difference in the performance between the three port simulations and the subsequent two and four port models indicates that while the dual source launcher couples roughly 70% of the incident power into the system, degraded electric field coupling results in power reflecting back and forth in the waveguide multiple times.

## 5.1 Future Work

Future endeavors in this area should focus on single sided calibration and power coupling. As seen in Chapter IV, the traditional error model for a single sided waveguide is incompatible with the dual source waveguide. As a result, the data calibrated with the three reflection standards is unusable. This implies that either a different set of standards should be developed for single sided calibration or that a source of error is not corrected with the calibration method.

Power coupling issues with the design are twofold. Coupling power into the system is problematic due to the impedance mismatch between the cable (or waveguide port)

and the excitation pin. This can be addressed with a number of solutions proposed including dielectric sheaths, tuning stubs, or excitation probe alterations. While multiple coax-to-waveguide structures were designed and simulated, no one design stood out from the rest. Each had unique trade offs. While coupling power into the system is inefficient so is coupling power out of the waveguide. The shape of the $E_y$ field of the dominant mode plays a key role in coupling power out of the waveguide. $TE_{10}$ power is much less efficient that $TE_{20}$ due to the excitation pins' placement at maxima of the $TE_{20}$ $E_y$ field.

# Appendix A. Nicolson-Ross-Weir Method

Nicolson and Ross initially proposed a broadband method for determining the complex relative permittivity and permeability of a sample of simple dielectric media with a single time-domain measurement [29]. A network analyzer interrogates a material under test with a sub-nanosecond pulse. The Fourier transform of the interrogation pulse, transmitted pulse, and reflected pulse yields transmission and reflection scattering parameters $S_{21}$ and $S_{11}$ in the frequency domain. From these calculated values the dielectric material properties are calculated. Taking advantage of the advent of more advanced network analyzers, Weir later improved on Nicolson's and Ross' technique [43]. The algorithm Weir proposes is summarized below along with adaptations contained in [6].

Once the transmission and reflection scattering parameters $S_{21}$ and $S_{11}$ are measured, the reflection factor $\Gamma$ is calculated with

$$\Gamma = \chi \pm \sqrt{\chi^2 - 1} \tag{60}$$

where

$$\chi = \frac{S_{11}^2 - S_{21}^2 + 1}{2S_{11}} \tag{61}$$

The proper root of Equation (60) is determined where $|\Gamma| < 1$ for passive materials. The intrinsic impedance of the dielectric material is

$$Z = \frac{1 + \Gamma}{1 - \Gamma} \tag{62}$$

The propagation factor of a wave propagating through a material is

$$P = \frac{S_{11} + S_{21} - \Gamma}{1 - (S_{11} + S_{21})\Gamma} = \frac{S_{21}}{1 - \Gamma S_{11}} \tag{63}$$

The propagation constant in a rectangular waveguide of interior width $a$ for $TE_{m0}$ modes is

$$\gamma_0 = \sqrt{k_x^2 - k_0^2} \tag{64}$$

where $k_x = \frac{m\pi}{a}$ and $k_0 = \omega\sqrt{\epsilon_0\mu_0}$. Finally, the relative permeability ($\mu_r$) and permittivity ($\epsilon_r$) of the material under test with a thickness $d$ are

$$\mu_r = \frac{-Z \cdot ln(P)}{\gamma_0 d} \tag{65}$$

$$\epsilon_r = \frac{k_x^2 - (\frac{ln(P)}{d})^2}{\mu_r k_0^2}. \tag{66}$$

## Appendix B. Single Excitation Single Sided Calibration

Single sided material measurements can be made with single or dual source excitation. In order to calibrate the single source excitation single sided measurements a linear model of the waveguide system is used.

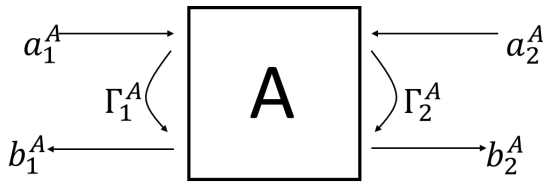


**Figure 26. Block model of the single sided waveguide measurement configuration.**

In Figure 26 port 1 is the network analyzer so that $\Gamma_1^A$ is $S_{11,p}^{ms}$ or the reflection coefficient at the network analyzer and port 2 is the waveguide aperture so that $\Gamma_2^A$ is $S_{11,p}^{s}$ which is the reflection coefficient at the waveguide aperture. $\Gamma_2^A$ is either a known value in the case of standard measurements or the value which is sought. From microwave system theory we know that

$$b_1^A = S_{11}^A a_1^A + S_{12}^A a_2^A \tag{67a}$$

$$b_2^A = S_{21}^A a_a^A + S_{22}^A a_2^A \tag{67b}$$

The aperture of the waveguide will always have a flat plate attached to it at some length, thus $a_2^A = b_2^A \Gamma_2^A$ which, when substituted into Equations (67a) and (67b) results in

$$b_1^A = S_{11}^A a_1^A + S_{12}^A b_2^A \Gamma_2^A \tag{68a}$$

$$b_2^A = S_{21}^A a_a^A + S_{22}^A b_2^A \Gamma_2^A \tag{68b}$$

Solving Equation (68b) for $b_2^A$ and then eliminating $b_2^A$ from Equation (68a) results

in $b_2^A = \frac{S_{21}^A a_1^A}{1-S_{22}^A \Gamma_2^A}$ and

$$
\begin{aligned}
b_1^A &= S_{11}^A a_1^A + S_{12}^A [\frac{S_{21}^A a_1^A}{1 - S_{22}^A \Gamma_2^A}] \Gamma_2^A \\
\frac{b_1^A}{a_1^A} = \Gamma_1^A &= S_{11}^A + \frac{S_{21}^A S_{12}^A \Gamma_2^A}{1 - S_{22}^A \Gamma_2^A} \\
S_{11,p}^{ms} &= S_{11}^A + \frac{S_{21}^A S_{12}^A S_{11,p}^S}{1 - S_{22}^A S_{11,p}^S}.
\end{aligned} \tag{69}
$$

Calibration requires the measurement of three independent standards in which a flat plate or electrical short is placed at different distances away from the aperture of the waveguide. This is accomplished with empty sample holders of different thicknesses. There are three unknown terms in Equation (69): $S_{11}^A$, $S_{21}^A S_{12}^A$, and $S_{22}^A$. By using reflection standards at different lengths, $S_{11,p}^S = -e^{j2k_{z0}L_s}$ where $k_z 0 = \sqrt[2]{k_0 - k_c^2}$, $k_0 = \omega/c$, $\omega = 2 * \pi * f$, $k_c = \frac{m\pi}{a}$, $m$ is the dominant mode number, $a$ is the waveguide width, and $L_s$ is the distance the flat plate is away from $z = 0$. In order to simplify the system of equations used in this calibration, the following parameterization is used:

$$M_{sh} = S_{11,p}^{mS,sh} \tag{70a}$$

$$K_{sh} = S_{11,p}^{sh} \tag{70b}$$

$$A = S_{11}^A \tag{70c}$$

$$B = S_{21}^A S_{12}^A \tag{70d}$$

$$C = S_{22}^A \tag{70e}$$

where $sh_{1,2,3}$ represents standards 1, 2, 3. These three standards are shorts placed at different lengths $(l_1, l_2, l_3)$ away from the waveguide aperture. This results in the following expressions for the measurements taken with the standards

$$M_1 = \frac{BK_1}{1 - CK_1} + A \tag{71a}$$

$$M_2 = \frac{BK_2}{1 - CK_2} + A \tag{71b}$$

$$M_3 = \frac{BK_3}{1 - CK_3} + A \tag{71c}$$

The difference of Equations (71a) and (71b) is

$$M_1 - M_2 = \frac{BK_1}{1 - CK_1} - \frac{BK_2}{1 - CK_2} = B(\frac{K_1 - K_2}{(1 - CK_1)(1 - CK_2)}) \tag{72}$$

which results in

$$B = \frac{(M_1 - M_2)(1 - CK_1)(1 - CK_2)}{K_1 - K_2}. \tag{73}$$

Similarly, the difference of Equations (71b) and (71c) is

$$\Delta M_{23} = \frac{BK_2}{1 - CK_2} - \frac{BK_3}{1 - CK_3} = B(\frac{K_2 - K_3}{(1 - CK_2)(1 - CK_3)}) \tag{74}$$

where $\Delta M_{mn} = M_m - M_n$ results in

$$B = \frac{(\Delta M_{23})(1 - CK_2)(1 - CK_3)}{\Delta K_{23}} \tag{75}$$

for $\Delta K_{mn} = K_m - K_n$.

The equations above for $B$ are used to solve for $C$ by setting Equation (74) equal

to Equation (75):

$$\begin{aligned}
\frac{(\Delta M_{12})(1-CK_1)(1-CK_2)}{\Delta K_{12}} &= \frac{(\Delta M_{23})(1-CK_2)(1-CK_3)}{\Delta K_{23}} \\
\frac{(\Delta M_{12})(1-CK_1)}{\Delta K_{12}} &= \frac{(\Delta M_{23})(1-CK_3)}{\Delta K_{23}} \\
\frac{\Delta M_{12}}{\Delta K_{12}} - \frac{(\Delta M_{12})CK_1}{\Delta K_{12}} &= \frac{\Delta M_{23}}{\Delta K_{23}} - \frac{(\Delta M_{23})CK_3}{\Delta K_{23}} \\
\frac{(\Delta M_{12})}{\Delta K_{12}} - \frac{\Delta M_{23}}{\Delta K_{23}} &= \frac{(\Delta M_{12})CK_1}{\Delta K_{12}} - \frac{(\Delta M_{23})CK_3}{\Delta K_{23}} \\
\frac{(\Delta M_{23})(\Delta K_{12}) - (\Delta M_{12})(K_2-K_3)}{(\Delta K_{12})(\Delta K_{23})} &= \left[\frac{(\Delta M_{23})(\Delta K_{12})K_3 - (\Delta M_{12})(\Delta K_{23})K_1}{(\Delta K_{12})(\Delta K_{23})}\right] C \\
C &= \frac{(\Delta M_{23})(\Delta K_{12}) - (\Delta M_{12})(\Delta K_{23})}{(\Delta M_{23})(\Delta K_{12})K_3 - (\Delta M_{12})(\Delta K_{23})K_1}
\end{aligned} \tag{76}$$

Once $C$ is calculated, Equations (74) or (75) are used to calculate $B$. With both $B$ and $C$ known, Equations (71a), (71a), or (71c) are used to calculate $A$. In order to calibrate the sample measurement $S_{11,p}^{msamp} = M_s$, Equation (69) must be rearranged using the nomenclature introduced in Equations (70a) - (70e), yielding

$$\begin{aligned}
M_s &= \frac{BK_s}{1-CK_s} + A \\
(M_s - A)(1-CK_s) &= BK_s \\
(M_s - A) - (M_s - A)CK_s &= BK_s \\
(M_s - A) &= (M_s - A)CK_s + BK_s \\
K_s &= \frac{M_s - A}{B + C(M_s - A)}
\end{aligned} \tag{77}$$

where $K_s = S_{11,p}^{samp}$ is the reflection coefficient of the sample. Newton's method for finding the root or zero of a function can now be used to find the relative permittivity of the sample as long as it is nonmagnetic.

The parameters $A$, $B$, and $C$ or $S_{11}^A$, $S_{21}^A S_{12}^A$, and $S_{22}^A$ characterize the waveguide and network analyzer when a specific port is active. This dependency has been suppressed for clarity, but only standard measurements made with a specific port can be used to calibrate sample measurements made with that same port. This process is repeated for each excitation port (i.e., ports 1 and 2 in terms of the proposed rectangular waveguide design in this research).

# Appendix C. Waveguide Drawings

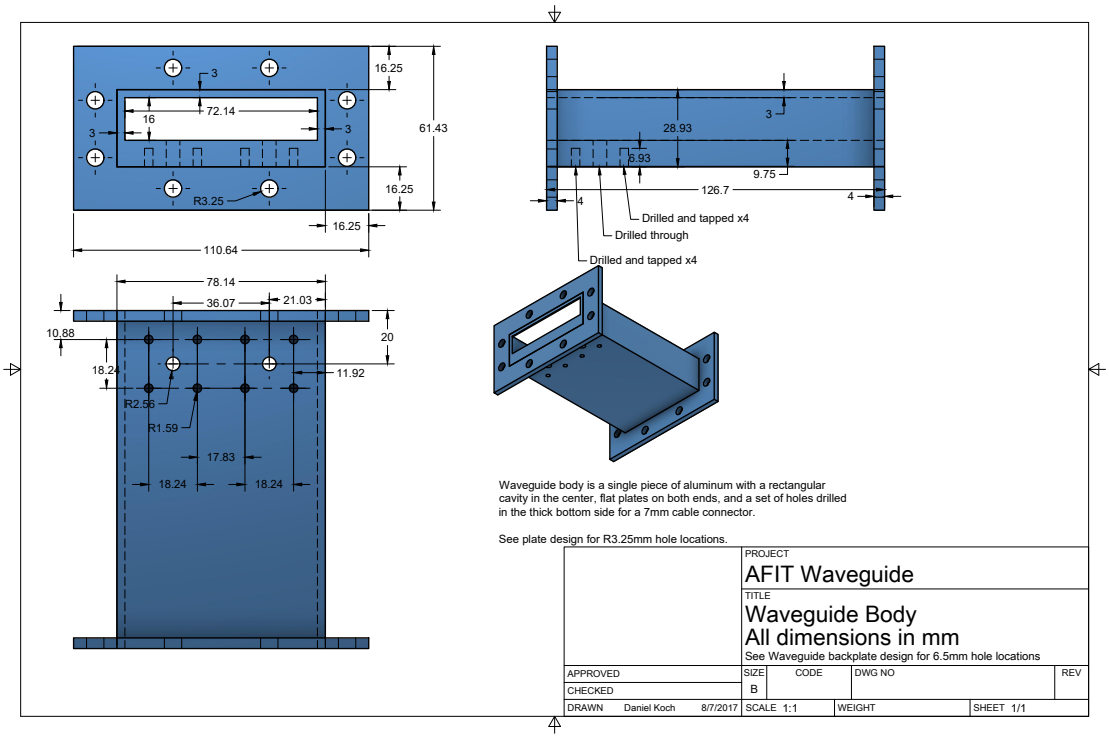


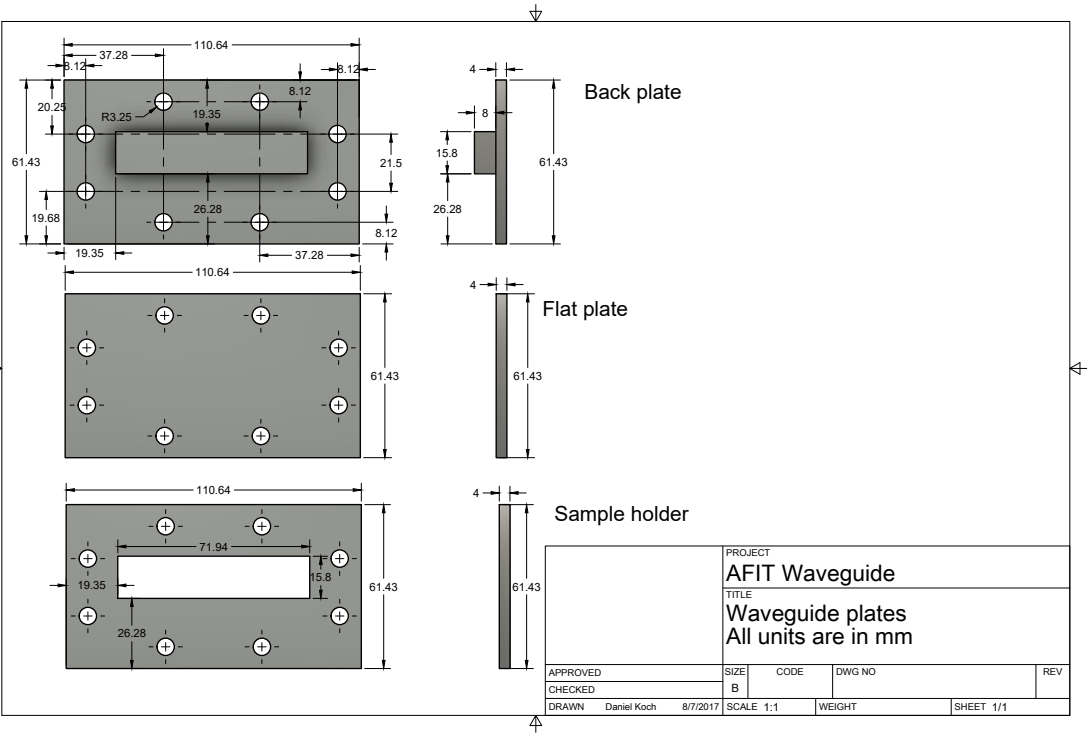

DWG NO. 311-07-00-000

NOTES:

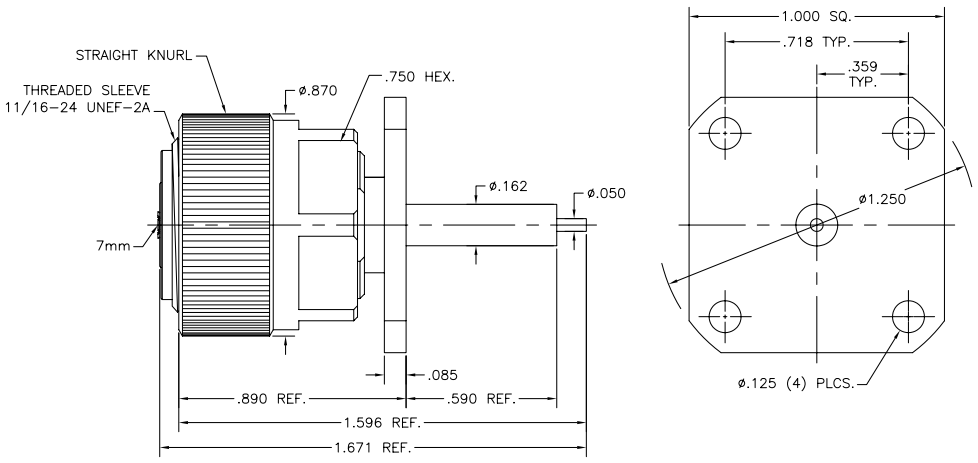


| | | | |
|---|---|---|---|
| DWG NO. 311-07-00-000 | **SGMC MICROWAVE** www.sgmcmicrowave.com | USED ON: *"OUTLINE DRAWING"* | REVISIONS |
| TITLE: 7mm CONNECTOR (4) HOLE FLANGE RECEPTACLE | SCALE: NTS \| CAGE CODE: 1UYM4 \| SIZE: A \| SHEET: 1 OF 1 \| DRAWN: LRH II \| APPR: | | |
| | UNLESS OTHERWISE SPECIFIED:<br>1. REMOVE ALL BURRS.<br>2. ALL DIMENSIONS ARE AFTER PLATING.<br>3. BREAK ALL CORNERS & EDGES .005 R. MAX.<br>4. CHAMFER 1st & LAST THREADS 45°.<br>5. DIAMETERS ON COMMON CENTERS SHALL BE CONCENTRIC WITHIN .002 T.I.R.<br>6. ALL SURFACES FINISHED TO 32√. | TOLERANCES<br>ALL DIMENSIONS ARE IN INCHES<br>"DECIMALS"<br>.X ±.030<br>.XX ±.010<br>.XXX ±.005 | FINISH:<br>MATERIAL: |

| LTR: | DESCRIPTION: (ECN#) | DATE: |
|---|---|---|
| -- | DWG. RELEASED | 01/07/02 |

# List of Abbreviations

| Abbreviation | | Page |
|---|---|---|
| MWS® | Microwave Studio® | iv |
| NRW | Nicolson-Ross-Weir | 1 |
| EDM | electrical discharge machining | 5 |
| AFIT | Air Force Institute of Technology | 5 |
| LOREnet | Low Observable Radar Electromagnetic Network | 5 |
| MWS® | Microwave Studio® | 5 |
| TPI | Triangle Precision Industries | 6 |
| SLA | stereolithography | 6 |
| TE | Transverse Electric | 8 |
| TM | Transverse Magnetic | 8 |
| TEM | Transverse Electromagnetic | 12 |
| PEC | Perfect Electric Conductor | 14 |
| CEM | computational electromagnetic | 28 |
| FDTD | finite difference time domain | 28 |
| MoM | method of moment | 28 |
| FEM | finite element method | 28 |
| TRL | Thru-Reflection-Line | 37 |
| RL | return loss | 40 |
| IL | Insertion loss | 40 |
| SWR | standing wave ratio | 41 |

# Bibliography


1. S. Arslanagić, T. V. Hansen, N. A. Mortensen, A. H. Gregersen, O. Sigmund, R. W. Ziolkowski, and O. Breinbjerg. A review of the scattering-parameter extraction method with clarification of ambiguity issues in relation to metamaterial homogenization. *IEEE Antennas and Propagation Magazine*, 55(2):91–106, 2013.

2. J. Baker-Jarvis, E. Vanzura, and W. Kissick. Improved technique for determining complex permittivity with the transmission/reflection method. *IEEE Transactions on Microwave Theory and Techniques*, 38(8):1096–1103, 1990.

3. C. Balanis. *Antenna Theory: Analysis and Design*. John Wiley & Sons, Inc., Hoboken, NJ, 3rd edition, 2005.

4. C Balanis. *Advanced Engineering Electromagnetics*. John Wiley & Sons, Inc., Hoboken, NJ, second edition, 2012.

5. D. Bockelman and W. Eisenstadt. Combined Differential and Common-Mode Scattering Parameters: Theory and Simulation. *IEEE Transactions on Microwave Theory and Techniques*, 43(7):1530–1539, 1995.

6. E. Buschelman. *Material Characterization Improvement in High Temperature Rectangular Waveguide Measurements*. PhD thesis, Air Force Instiute of Technology, 2007.

7. N. Carmel, D. Elmakayes, and H. Matzner. Investigation of a coax-to-waveguide transition element. *2011 IEEE International Conference on Microwaves, Communications, Antennas and Electronic Systems, COMCAS 2011*, (1):2–4, 2011.

8. R. Cravey, M. Deshpande, D. Reddy, and P. Tiemsin. Evaluation of Complex Permittivities of Multilayer Dielectric Substrates at Microwave Frequencies Using Waveguide Measurements. In *AMTA*, 1996.

9. N. Damaskos, R. Mack, A. Maffett, W. Parmon, and P. Uslenghi. The Inverse Problem for Biaxial Materials. *IEEE Transactions on Microwave Theory and Techniques*, 32(4):400–405, 1984.

10. A. De Paula, M. Rezende, and J. Barroso. Modified Nicolson-Ross-Weir (NRW) method to retrieve the constitutive parameters of low-loss materials. *SBMO/IEEE MTT-S International Microwave and Optoelectronics Conference Proceedings*, pages 488–492, 2011.

11. M. Durga, S. Tomar, S. Singh, and L. Suthar. Millimeter wave in-line coaxial-to-rectangular waveguide transition. *2011 IEEE Applied Electromagnetics Conference, AEMC 2011*, pages 5–7, 2011.

12. G. Engen and C. Hoer. Thru-Reflect-Line: An Improved Technique for Calibrating the Dual Six-Port Automatic Network Analyzer, 1979.

13. W. Feng, W. Che, and Q. Xue. The proper balance: Overview of microstrip wideband balance circuits with wideband common mode suppression. *IEEE Microwave Magazine*, 16(5):55–68, 2015.

14. D. Frickey. Conversions Between S, Z, Y, h, ABCD, and T Parameters which are Valid for Complex Source and Load Impedances. *IEEE Transactions on Microwave Theory and Techniques*, 42(2):205–211, 1994.

15. U. Hasar, J. Barroso, C. Sabah, I. Ozbek, and Et. Al. Retrieval Of Effective Electromagnetic Parameters Of Isotropic Metamaterials Using Reference-Plane Invariant Expressions. *Progress In Electromagnetics Research-Pier*, 132(October):425–441, 2012.

16. M. Havrilla, A. Bogle, and M. Hyde. Improved Bandwidth in Rectangular Waveguide Material Characterization Measurements. *AMTA 36th Annual Meeting and Symposium*, (September):6–11, 2014.

17. A. Huynh, P. Hakansson, and S. Gong. Mixed-mode S-parameter conversion for networks with coupled different signals. *European Microwave Conference*, 2007.

18. M. Hyde and M. Havrilla. Multimode Analysis of a One-Port Dual Ridged Waveguide Probe. *87th ARFTG Microwave Measurement Conference: Measurements for Emerging Communications Technologies, ARFTG 2016*, pages 0–3, 2016.

19. J. Jarem. A Multifilament Method-of-Moments Solution for the Input Impedance of a Probe-Excited Semi-Infinite Waveguide. *IEEE Transactions on Microwave Theory and Techniques*, 35(1):14–19, 1987.

20. R. Johnston and T. Choi. Coax to waveguide transition optimization using wire/-plate method of moments. *1998 Midwest Symposium on Circuits and Systems (Cat. No. 98CB36268)*, pages 276–279, 1998.

21. R. Keam and A. Williamson. Analysis and Design of Coaxial-Line/Rectangular Waveguide Junction with a Dielectrically Sheathed Centre Probe. 1992.

22. A. Knisley. Biaxial Anisotropic Material Development and Characterization using Rectangular to Square Waveguide. In *9th International Congress on Advanced Electromagnetic Materials in Microwaves and Optics - Metamaterials*, number September, page 104, 2015.

23. D. Koch and M. Havrilla. Broadband Rectangular Waveguide Launcher Design Using Dual Source Excitation. In *2018 European Conference on Antennas and Propagation, EuCAP*, 2018.

24. E. Kreyszig. *Advanced Engineering Mathematics*. John Wiley & Sons, Inc., Hoboken, NJ, 10th edition, 2011.

25. S. Mahmoud. *Electromagnetic Waveguides: Theory and Applications*, volume 4. The Institution of Engineering and Technology, London, U.K., 2006.

26. N. Marcuvitz. *Waveguide Handbook*, volume 33. The Institution of Engineering and Technology, London, U.K., 1987.

27. R. Marks. Formulations of the Basic Vector Network Analyzer Error Model including Switch-Terms. *50th ARFTG Conference Digest*, 32:115–126, 1997.

28. D. McNarma, C. Pistorius, and J. Malherbe. *The Uniform Geometric Theory of Diffraction*. Artech House, Norwood, MA, 1990.

29. A. Nicolson and G. Ross. Measurement of the Intrinsic Properties of Materials by Time-Domain Techniques. *IEEE Transactions on Instrumentation and Measurement*, 19(4):377–382, 1970.

30. D. Otto. The Admittance of Cylindrical Antennas Driven From a Coaxial Line. *Radio Science*, 2(9):1031–1042, 1967.

31. D. Pozar. *Microwave Engineering*. John Wiley & Sons, Inc., Hoboken, NJ, 3rd ed. edition, 2005.

32. M. Richards, J. Scheer, and W. Holm. *Principles of Modern Radar*. SciTech Publishing, Inc, Raleigh, NC, 2010.

33. J. Rollins and J. Jarem. The Input Impedance of a Hollow-Probe-Fed, Semi-infinite Rectangular Waveguide. *IEEE Transactions on Microwave Theory and Techniques*, 37(7):1144–1146, 1989.

34. Y. Rong and K. Zaki. Characteristics of generalized rectangular and circular ridge waveguides. *IEEE Transactions on Microwave Theory and Techniques*, 48(2):258–265, 2000.

35. D. Rytting. An Analysis of Vector Measurement Accuracy Enhancement Techniques. In *RF & Microwave Symposium and Exhibition*, 1982.

36. D. Rytting. Network Analyzer Error Models and Calibration Methods. *White Paper, September*, pages 1–44, 2008.

37. P. Saha and D. Guha. Bandwidth and dispersion characteristics of a new rectangular waveguide with two L-shaped septa. *IEEE Transactions on Microwave Theory and Techniques*, 47(1):87–92, 1999.

38. J. Stewart and M. Havrilla. Electromagnetic Characterization of a Magnetic Material Using an Open-ended Waveguide Probe and a Rigorous Full-wave Multimode Model. *Journal of Electromagnetic Waves and Applications*, 20(14):2037–2052, 2006.

39. N. Tako, E. Levine, G. Kabilo, and H. Matzner. Investigation of thick coax-to-waveguide transitions. In *8th European Conference on Antennas and Propagation, EuCAP 2014*, pages 908–911, 2014.

40. A. von Hippel. *Dielectric Materials and Applications*. MIT Press, Cambridge, MA, 1961.

41. P. Wade. Rectangular Waveguide to Coax Transition Design. *Qex*, pages 10–17, 2006.

42. K. Warnick. *Numerical Methods for Engineering*. SciTech Publishing, Inc, Edison, NJ, 2011.

43. W. Weir. Automatic Measurement of Complex Dielectric Constant and Permeability. *Proceedings of the IEEE*, 62(1):33–36, 1974.

44. A. Williamson and D. Otto. Cylindrical Antenna in a Rectangular Waveguide Driven from a Coaxial Line. *Electronics Letters*, 8(22):545–547, 1972.

# REPORT DOCUMENTATION PAGE

*Form Approved*
*OMB No. 0704-0188*



**PLEASE DO NOT RETURN YOUR FORM TO THE ABOVE ADDRESS.**

| 1. REPORT DATE *(DD-MM-YYYY)* | 2. REPORT TYPE | 3. DATES COVERED *(From - To)* |
|---|---|---|
| 22 Mar 2018 | Master's Thesis | Sep 2016 - Mar 2018 |

**4. TITLE AND SUBTITLE**

Dual Source Excitation Rectangular Waveguide Design and Evaluation for the Measurement of Electromagnetic Material Properties

**5a. CONTRACT NUMBER**

**5b. GRANT NUMBER**

**5c. PROGRAM ELEMENT NUMBER**

**6. AUTHOR(S)**

Koch, Daniel K., Capt, USAF

**5d. PROJECT NUMBER**

JON 18G165

**5e. TASK NUMBER**

**5f. WORK UNIT NUMBER**

**7. PERFORMING ORGANIZATION NAME(S) AND ADDRESS(ES)**

Air Force Institute of Technology
Graduate School of Engineering and Management (AFIT/EN)
2950 Hobson Way
Wright-Patterson AFB OH 45433-7765

**8. PERFORMING ORGANIZATION REPORT NUMBER**

AFIT-ENG-MS-18-M-039

**9. SPONSORING/MONITORING AGENCY NAME(S) AND ADDRESS(ES)**

Air Force Research Laboratory, Sensors Directorate
Attn: Garrett Stenholm
2591 K St, Bldg 254
WPAFB, OH 45433-7602
DSN: 785-9175 Email: Garrett.Stenholm@us.af.mil

**10. SPONSOR/MONITOR'S ACRONYM(S)**

AFRL/RYS

**11. SPONSOR/MONITOR'S REPORT NUMBER(S)**

**12. DISTRIBUTION/AVAILABILITY STATEMENT**

Distribution Statement A. Approved for Public Release; Distribution Unlimited

**13. SUPPLEMENTARY NOTES**



**14. ABSTRACT**

Broadband material parameter measurements are essential in understanding how materials interact with electromagnetic waves. Traditional rectangular waveguide material measurement systems are bandwidth limited. Efforts to produce a broadband rectangular waveguide have focused on the inclusion of different guiding structures in the waveguide body. These designs require precise machining and time-consuming sample preparation. This research proposes a broadband rectangular waveguide design which uses a dual source excitation design. The fields excited by each source superimpose in a linear fashion resulting in the suppression of unwanted higher order electromagnetic modes. A dual source excitation waveguide is proposed in this research. Results from CST Microwave Studio simulations are compared with those from a physical design measured with a 2-port network analyzer. These results are used to determine if this proposed rectangular waveguide design is suitable for broadband material measurements.

**15. SUBJECT TERMS**

Rectangular Waveguide, RF Material Measurement, Electromagnetics, Mixed Mode Design

| 16. SECURITY CLASSIFICATION OF: | | | 17. LIMITATION OF ABSTRACT | 18. NUMBER OF PAGES | 19a. NAME OF RESPONSIBLE PERSON |
|---|---|---|---|---|---|
| a. REPORT | b. ABSTRACT | c. THIS PAGE | | | Dr. Michael J. Havrilla, AFIT/ENG |
| U | U | U | UU | 98 | 19b. TELEPHONE NUMBER *(Include area code)* (937) 255-3636 x4582 michael.havrilla@afit.edu |